# Modeling Sediment Fluxes from Debris-Rich Basal Ice Layers

**Ethan Pierce[1,2], Irina Overeem[1,2], Guillaume Jouvet[3]**

[1]Institute of Arctic and Alpine Research, Boulder, CO, USA
[2]Department of Geological Sciences, University of Colorado Boulder, USA
[3]Institute of Earth Surface Dynamics, Université de Lausanne, Switzerland

**Key Points:**

- We develop a model of sediment entrainment beneath an alpine glacier to predict sediment fluxes and basal ice stratigraphy at the terminus
- The model explains the co-occurrence of solid, debris-rich ice layers and overlying dispersed basal ice facies observed at glacier margins
- We model sediment fluxes and the thickness of debris-rich basal ice layers over a range of velocity and pressure configurations

Corresponding author: Ethan Pierce, `ethan.pierce@colorado.edu`

## Abstract

Sediment erosion, transport, and deposition by glaciers and ice sheets plays a crucial role in shaping landscapes, provides important nutrients to downstream ecosystems, and preserves key indicators of past climate conditions in the geologic record. While previous work has quantified sediment fluxes from subglacial meltwater, we also observe sediment entrained within basal ice, transported by the flow of the glacier itself. However, the formation and evolution of these debris-rich ice layers remains poorly understood and rarely represented in landscape evolution models. Here, we identify a characteristic sequence of basal ice layers at Mendenhall Glacier, Alaska. We develop a numerical model of frozen fringe and regelation processes that describes the co-evolution of this sequence and explore the sensitivity of the model to key properties of the subglacial sedimentary system, using the Instructed Glacier Model to parameterize ice dynamics. Then, we run numerical simulations over the spatial extent of Mendenhall Glacier, showing that the sediment transport model can predict the observed basal ice stratigraphy at the glacier's terminus. From the model results, we estimate basal ice layers transport between 23,256 $m^3$ $a^{-1}$ and 39,810 $m^3$ $a^{-1}$ of sediment, mostly entrained in the lowermost ice layers nearest to the bed, and varying strongly with the effective pressure at the ice-till interface. Overall, our results suggest that glacial sediment transport depends on complex interactions between till, hydrology, and ice dynamics, and show that sediment entrainment in basal ice likely represents a substantial component of the total sediment transport budget of most alpine glaciers.


## Plain Language Summary

Glaciers shape landscapes by eroding mountain ranges and moving the eroded sediment downstream to the lakes, fjords, and other ecosystems near the terminus. To quantify this supply of sediment, and thus understand the evolution of high alpine landscapes, we often use numerical models to simulate the processes of erosion and transport. Previous work has focused on the role of meltwater channels underneath glaciers to transport sediment, analogous to how rivers move sediment across much of Earth's surface, but we also know from field observations that a portion of the underlying sediment is picked up and incorporated into the ice itself. Here, we develop a new model to simulate where and how sediment is incorporated into ice beneath the glacier, and how those debris-rich ice layers are modified as the glacier flows downstream. We use this model to predict the total amount of sediment reaching a glacier's snout, as well as the spatial distribution and thickness of the debris-rich ice. Our results show that the amount of sediment transported in glacier ice likely represents a significant component of the total amount of sediment eroded or transported by the glacier, and thus should not be ignored in broader models of landscape evolution.

## 1 Introduction

Across the cold regions of Earth's surface, glaciers are active geomorphic agents, efficiently eroding bedrock and transporting available sediment downstream (Delmas et al., 2009; Alley et al., 2019; Cook et al., 2020). While much of this material is transported by meltwater running beneath the glacier (Hodson & Ferguson, 1999; Swift et al., 2005; Delaney & Adhikari, 2020), we also observe visually-distinct layers of sediment entrained in ice near the base of many glaciers and ice sheets. Often seen at the termini of alpine glaciers, the collapsed margins of ice sheets, within the walls of ice caves, and even atop overturned icebergs, the striking, dark colors of these debris-rich ice layers form a stark contrast with the clean, white or blue glacier ice above them (Post & LaChapelle, 2000). The sediment within these layers can be composed of anything from fine glacial flour to head-sized boulders, creating imposing structures of meters or more in height within the glacier ice. This sediment supply may represent a substantial source of material to fjords

and periglacial landscapes and ecosystems (Syvitski et al., 1996; Knight et al., 2002; Riihimaki et al., 2005; Cook, Swift, et al., 2011; Overeem et al., 2017), especially at the glacier terminus, where it contributes to the construction of terminal moraines and grounding zone wedges (Alley et al., 2007; Batchelor & Dowdeswell, 2015; Rowan et al., 2022). However, the physical processes that form these debris-rich ice layers remain poorly understood and are rarely invoked in geomorphic models of glacial landscape evolution.

To help understand the role of basal ice in transporting sediment across a landscape, we have observations from glacio-stratigraphic field studies at the margins of glaciers and ice sheets. Previous efforts have focused on describing basal ice facies: characteristic properties of a layer of ice and sediment that are unique to a particular entrainment process (Knight, 1994, 1997; Hubbard et al., 2009). More recent work has focused on translating these descriptions of basal ice layers into standardized classifications of *cryofacies* (Evans & Benn, 2014; Hubbard et al., 2009). In glaciers across the world, we observe a common sequence of two distinct cryofacies: a solid or solid-stratified facies near the ice-bed interface, and a dispersed facies directly above it (Lawson, 1979; Knight, 1997; Cook, Graham, et al., 2011). According to Hubbard et al.'s classification scheme (Hubbard et al., 2009), both of these units are primarily structureless, although they may exhibit weak layering at centimeter-decimeter scales. The solid cryofacies may be decimeters to meters thick, and is composed of frozen debris with interstitial ice. Above this unit, typically separated by a diffuse contact, the dispersed layer may present as either a dispersed stratified or a dispersed banded cryofacies (Hubbard et al., 2009; Cook, Swift, et al., 2011). Both of these cryofacies can be meters to even tens of meters thick (Lawson, 1979; Cuffey et al., 2000; Cook, Graham, et al., 2011), contain bubble-free ice with low-to-intermediate sediment concentrations, and consist of finer particles and aggregates of multiple particles (Hubbard et al., 2009). While previous models of basal sediment transport only focus on the highly-concentrated, lowermost layer of frozen-on debris (Iverson, 1993; Hildes et al., 2004; Meyer et al., 2019), recent work has shown that the overlying dispersed layers may transport a comparable flux of sediment (Cook, Swift, et al., 2011). While this two-sequence facies is prevalent in many glacial systems and represents a significant contribution of sediment to the glacier terminus (Lawson, 1979; Knight, 1997; Cook, Graham, et al., 2011), there are currently no process models that describe and quantify the co-evolution of solid and dispersed basal ice facies.

Theoretical advances and laboratory experiments indicate that there are several processes that entrain and distribute sediment within basal ice layers. When a glacier rests on an unlithified bed, ice infiltrates the substrate and accretes a layer of frozen sediment at the glacier sole (Iverson, 1993; Rempel, 2008; Meyer et al., 2021). This process initiates when the effective pressure (the difference between ice overburden pressure and the water pressure beneath a glacier) becomes great enough to overcome the resistance posed by films of liquid water bridging the space between sediment particles. This *frozen fringe* consists of debris and interstitial ice, where the entire matrix has been frozen onto the base of the glacier. The expression of the frozen fringe is thus consistent with descriptions of solid or solid stratified cryofacies. In turn, the thermodynamics within the frozen fringe create the necessary conditions for the formation of an overlying dispersed facies. Sediment particles in an ice matrix migrate through the process of *regelation*, where ice partially melts around the grain to form a micron-scale film of liquid water (Iverson, 1993; Rempel et al., 2004). When subjected to a gradient in pressure and/or temperature, the particle will gradually move towards regions of lower pressure and warmer temperature, respectively (Wettlaufer & Worster, 2006). To create meters-scale layers of dispersed sediment, however, the process of regelation requires a steady supply of material already emplaced in the ice mass and a macroscopic gradient in pressure and/or temperature in the basal ice layers. The frozen fringe supplies both of these needs, ensuring particles are entrained into the base of the ice mass, and due to the thermodynamics of partial freezing and melting, there will always be a slight depression in temperature at the top of the fringe (Rempel, 2008; Meyer et al., 2019, 2021). As such, the de-

velopment of frozen fringe and particle regelation are a plausible model for the co-evolution of solid and dispersed basal ice facies in a wide variety of glacial settings.

Sediment supply from entrainment and transport in basal ice layers has the potential to represent an important source of material to periglacial landscapes, but only coarse estimates of the magnitude of this flux exist (Syvitski et al., 1996; Cook, Swift, et al., 2011; Overeem et al., 2017). The physical mechanisms responsible for this sediment supply have been studied in isolation (Rempel, 2008; Meyer et al., 2019; You et al., 2021), but have not been combined into a comprehensive process model that can be coupled with geomorphic models of landscape evolution. In this study, we use field observations from Mendenhall Glacier, near Juneau, Alaska, to inform the development of a process model of subglacial sediment entrainment and transport. We provide field observations from the land-terminating section of the glacier's terminus, demonstrating that the basal ice layers at this location exhibit a sequence of both solid and dispersed basal ice facies. To quantify the evolution of these observed basal ice facies, we outline a model for sediment entrainment by frozen fringe and regelation, including general governing equations to couple with existing thermomechanical ice sheet models. We then explore the sensitivity of sediment entrainment processes to key input parameters. Finally, we provide a coupled model of sediment entrainment and ice flow for Mendenhall Glacier, and discuss the relevance of this approach to other glaciological settings. Our results show that basal ice layers depend strongly on effective pressure, the spatial distribution and magnitude of basal sliding, and the properties of the underlying till. The model results are broadly consistent with field observations, and allow us to predict both the observed basal ice stratigraphy at the terminus and estimate the overall sediment flux transported by basal ice layers.

## 2 Field observations

### 2.1 Geologic background

Located just north of Juneau, Alaska, at 58° N, Mendenhall Glacier is a typical tidewater glacier for southeast Alaska (Figure 1b). Juneau's climate is subarctic-maritime, with a mean annual temperature slightly above 1° C and an average of 230 days of precipitation, including 4.5 m of snow (Powell et al., 2022). Decreasing snow accumulation and increasing air temperatures have caused Mendenhall Glacier to retreat by about 3 km over the past century, exposing a proglacial lake (Motyka et al., 2003). Connected at its northern margin to the Juneau Icefield, the glacier begins at an ice divide around 1600 m (Pfeffer et al., 2014; Porter et al., 2022). It flows for nearly 23 km, with most sections of the main stem between 1.3 and 1.8 km in width. The maximum ice thickness is approximately 500 m (Farinotti et al., 2021), with a total glaciated area of 109 km$^2$. Surface velocities in Mendenhall Glacier's main stem approach 150 m a$^{-1}$, with velocities decreasing towards the terminus (A. Gardner et al., 2022). The last 500 m of the glacier's main stem is projected to sit below sea level (Porter et al., 2022), and its margin is split between Mendenhall Lake and a terminal moraine. While the glacier's calving front has been at or near flotation in the past, it has most likely grounded on a bedrock ridge in the past several years (Motyka et al., 2003). Towards the Juneau Icefield, the glacier is underlain by the Coast metamorphic-plutonic complex, including the tonalitic Mendenhall Glacier pluton (Wilson et al., 2015). In contrast, the lower portion of the glacier overrides more erodible metasedimentary rocks from the Yukon-Tanana and Taku terranes and glacial till (Wilson et al., 2015).

### 2.2 Field observations

To investigate basal ice facies at Mendenhall Glacier, we conducted a field survey of the section of the glacier's terminus that has grounded on its terminal moraine as of August 2021 (Figure 1). At well-spaced intervals across the 500 m of accessible termi-

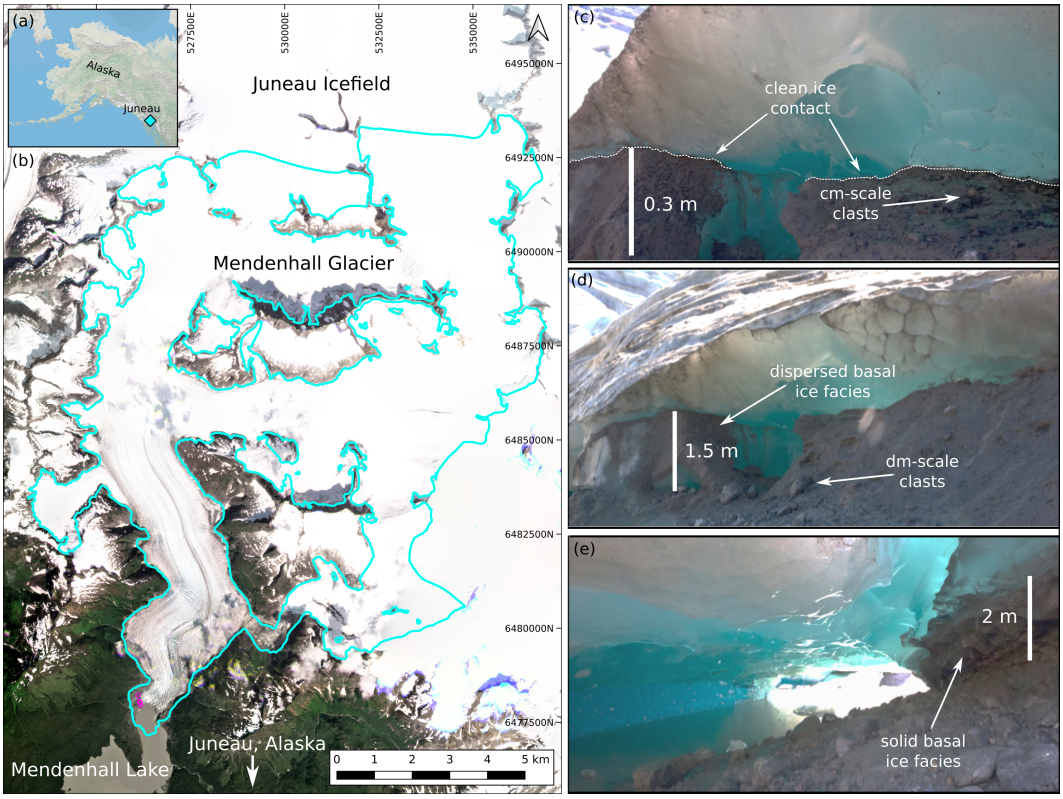


**Figure 1.** Overview map of Mendenhall Glacier. An inset map (a) shows the glacier's location within Alaska. Left (b), the glacier outline from the Randolph Glacier Inventory v6.0 (Pfeffer et al., 2014) (teal) is plotted on a Planetscope Visual Basemap from August 2021 (Planet Labs PBC) (Team, 2017). Field sampling locations are indicated by magenta points near the glacier's terminus. Right (c-e), three photos of basal ice exposures show the sharp contact between debris-rich and clean ice, with approximate scale bars and field facies description.

nal ice, we identified five representative columns of exposed basal ice layers. We recorded qualitative observations of ice properties: including color, clarity, bubble size and spacing, and deformation signatures, as well as sediment properties: including sorting, largest clast size, angularity, and spacing within the ice. We measured the total height of debris-rich ice and the thickness of any internal layers.

To quantitatively measure the sediment concentrations in basal ice layers, we obtained samples of ice and entrained sediment at vertical intervals within the column, with duplicate samples taken at 1 m horizontal spacing from the same height above the bed. To avoid artificial enrichment from surface melting, we first removed the outer 1-3 cm of ice and sediment before sampling. We measured total sample weight in the field, then shipped the samples back to the Sedimentology lab at INSTAAR. Samples were freeze-dried in a VirTis BenchTop "K" Series Freeze Dryer to sublimate away the melted ice, then the sediment fraction was weighed to obtain sediment concentration.

### 2.3 Basal ice facies

We found ubiquitous debris-rich basal ice layers across the entire land-terminating portion of Mendenhall Glacier's margin (Figure 2). This section of the terminus is tilted

upwards at a 24-32° angle, such that true thicknesses for the debris-rich ice layers were 1.6 - 2 m across the margin. Because the glacier appears to thrust onto its terminal moraine, it is unlikely that we sampled all the way down to the ice-bed interface anywhere along the margin. At the lowest point in each column, we observed more pronounced internal layers, with closer spacing, larger clast sizes, and a diffuse contact with massive, structureless debris layers above. At the top of each debris-rich ice layer, we observed a sharp contact with the overlying clean ice. We did not identify evidence of widespread deformation or folding within basal ice layers, but bubbles within the lowest 1 m of the ice matrix sometimes exhibited elongated, sheared profiles.

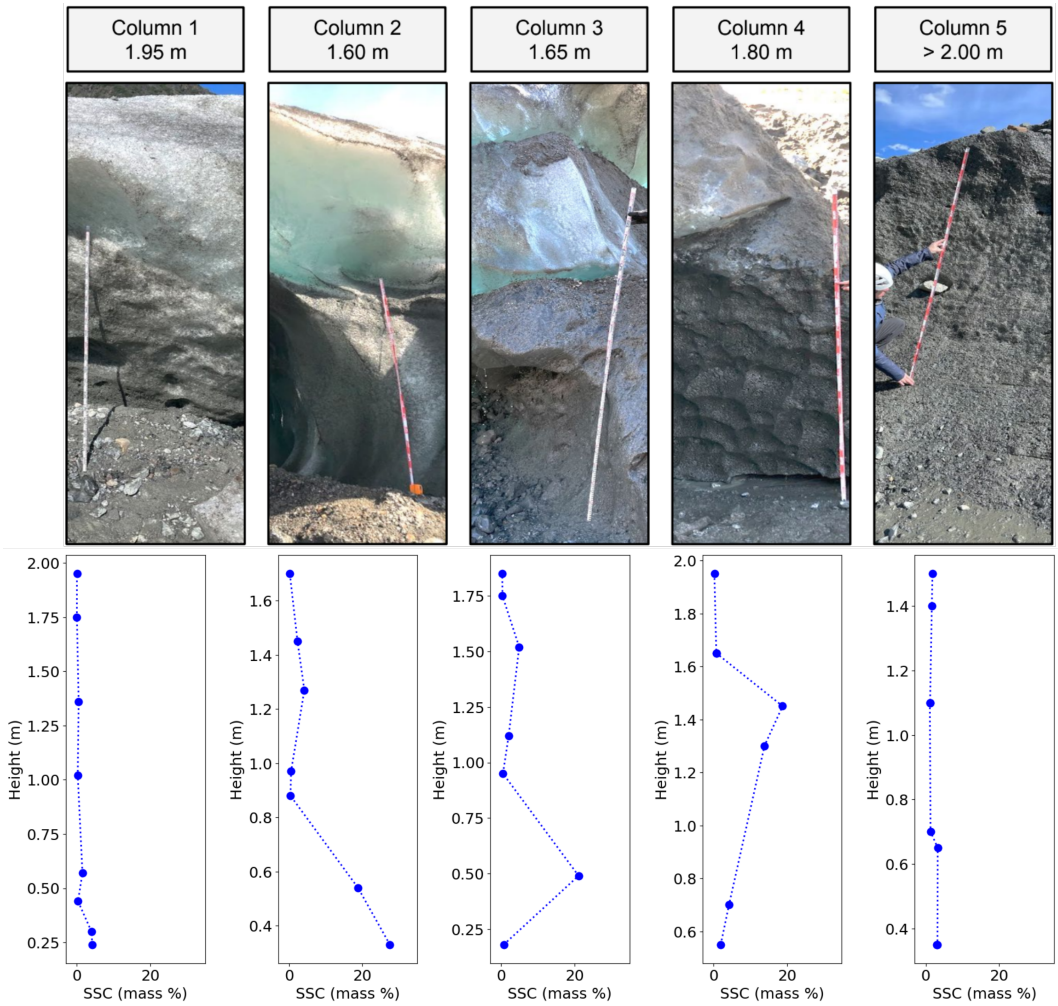


**Figure 2.** Photographs of sampled basal ice exposures. Total column thicknesses range from 1.6 m to over 2 m and sediment concentrations through each layer are plotted below.

The majority of our measured sediment concentrations are low, between 1% and 5% by mass, with a general pattern of high sediment concentrations near the base, decreasing upwards in the ice column (Figure 2). At columns 1 and 5, sediment concentrations are 3-4% at the base, with increased stratification of internal layers near the bed. Columns 2 and 3 exhibit elevated sediment concentrations of 20-25% in their lowermost layers. Column 4 is anomalous, with low sediment concentrations near the bed and no stratification below 1.4 m in the ice column. Aside from column 4, we observe uniformly

low sediment concentrations and no internal organization above 0.5 m from the base. We do not see any trends in angularity, sorting, or grain size between samples at different heights or in different locations. The sampled sediment is angular or sub-angular and poorly sorted, with grain sizes ranging from fine silt to 30 cm cobbles. In the field, we found several large cobbles emplaced at 2 m above the bed, either within basal ice layers or the overlying clean ice facies.

### 2.4 Facies interpretations

Based on our qualitative descriptions and measured sediment concentrations, we delineate a sequence of two distinct basal ice facies at Mendenhall Glacier. Closest to the bed, we describe a solid stratified or stratified solid facies (Hubbard et al., 2009), depending on the exposure. For ease, we will call both of these solid facies, as they are both characterized by high sediment concentrations ($> 20\%$ by mass), a greater prevalence of large clasts, and no bubbles within the interstitial ice. Above that layer, we describe a dispersed or dispersed stratified layer (Hubbard et al., 2009), both of which we will refer to as a dispersed facies. Despite its visual appearance as distinct from clean ice, this layer has lower sediment concentrations (1-5% by mass), and is further characterized by a massive internal structure, relatively more fine particles and clusters, and bubbles spaced at decimeter to centimeter scales within the ice matrix. Collectively, this two-facies sequence composes the vast majority of exposed basal ice layers at Mendenhall Glacier's land-terminating margin.

## 3 Model development

Here, we describe a process framework for sediment entrainment beneath glaciers and ice sheets that explains the co-evolution of solid and dispersed basal ice facies. We work from the base upwards, first describing the evolution of frozen fringe beneath an ice mass, then discussing the regelation of individual particles in the ice above the fringe. We then describe implementation details, making note of key simplifying assumptions. Figure 3a shows a schematic overview of the mechanism(s) we incorporate into the sediment entrainment model, and Table 1 provides relevant variable names, notation, and units. We have developed an open source Python implementation of the model within the Landlab framework (Barnhart et al., 2020).

### 3.1 Frozen fringe

#### *3.1.1 Initiation criterion*

Below an ice mass, the pressure of the overlying ice, $P_i$, is resisted by water pressure, $P_w$, beneath it. When the effective pressure, denoted by $N \equiv P_i - P_w$, is greater than a critical value $N_0$, ice begins to infiltrate the underlying material. This critical effective pressure is set by the surface energy, $\gamma$, of the films of water that form around particles in the substrate, and the radius of curvature between sediment grains, $r_c$ (Rempel, 2008; Meyer et al., 2019):

$$N_0 = \frac{\gamma}{r_c}. \tag{1}$$

We typically approximate the radius of curvature as equal to some characteristic sediment grain size, such that infiltration can occur even at relatively low effective pressures (Table 1).

#### *3.1.2 Fringe evolution*

Once ice infiltrates underlying material, a frozen fringe evolves based on the balance between the basal melt rate and the infiltration rate, and is advected downstream by ice flow. Here, we briefly reproduce the key physical equations that govern frozen fringe

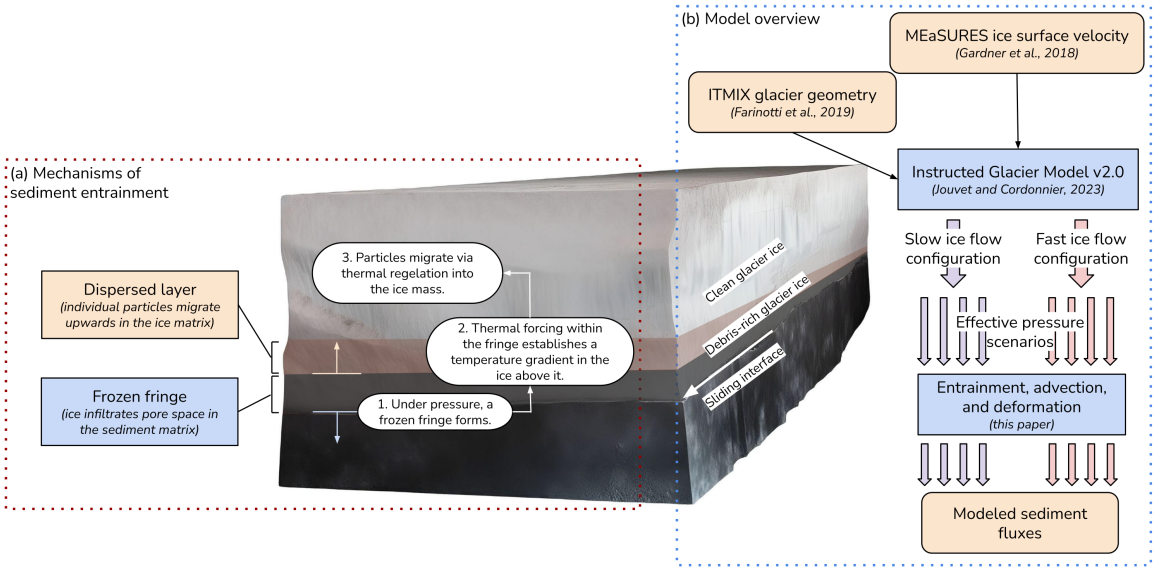


**Figure 3.** Schematic description of the model. Panel (a) shows the spatial relationship between the frozen fringe (§3.1) and dispersed layers (§3.2), with vertical arrows indicating the direction of movement for each interface. Panel (b) shows the flow of information through our coupled model framework: input data products are used in conjunction with IGM (§4.2) to generate a range of realistic scenarios, which are then run through a fully coupled entrainment-advection model to predict sediment fluxes at the glacier terminus. The base image is for illustrative purposes only, not drawn to scale, generated with the use of Midjourney AI.

evolution, and refer to (Rempel, 2008) and (Meyer et al., 2021) for further detail. Not yet considering the role of advection, the frozen fringe thickness $H_f$ follows a rate balancing equation:

$$\frac{\partial H_f}{\partial t} = \frac{-m_b - V}{\phi \bar{S}}, \tag{2}$$

where $m_b$ is the rate of basal melt, $V$ is the vertical motion of sediment due to the heave force and ice infiltration, $\phi$ is the porosity of the sediment, and $\bar{S}$ is the depth-averaged saturation of ice within the fringe (Table 1). When $V$ is negative, ice infiltration outpaces downwards heave of the sediment particles; if this rate outpaces the rate of ice loss due to basal melt, the frozen fringe will grow.

Here, we estimate subglacial melt as a combination of geothermal and frictional heat fluxes:

$$m_b = \frac{1}{\rho_i L} \left( Q_g + u_b \tau_b \right) \tag{3}$$

where $\rho_i$ is the ice density, $L$ is the latent heat of ice, $Q_g$ is the geothermal heat flux, and the product of sliding velocity and shear stress, $u_b \tau_b$, is the frictional heat flux. In doing so, we assume there is minimal heat loss to the overlying ice due to conduction. This assumption is likely valid for temperate glaciers, but may not hold for cold or polythermal glaciers, where large differences in temperature between the base of the glacier and the interior ice may lead to pronounced temperature gradients and large conductive heat fluxes (Blatter & Hutter, 1991; Aschwanden et al., 2012; Hewitt & Schoof, 2017).

Because development of a frozen fringe requires an unlithified bed below it, we assume that till deformation plays a role in modulating the shear stress at the ice-bed interface (Iverson et al., 1999; Hansen & Zoet, 2022). In soft-bed slip laws, shear stress is modeled as a bounded function of effective pressure, sliding velocity, and the properties of the underlying sediment (Schoof, 2010; Zoet & Iverson, 2020; Zoet et al., 2021). We use the formulation from (Zoet & Iverson, 2020), where:

$$\tau_b = N \, tan(\varphi) \left[ \frac{u_b}{u_b + u_t} \right]^{1/p}, \tag{4}$$

for friction angle $\varphi$, threshold velocity $u_t$, and empirical parameter $p = 5$. The threshold velocity depends on till grain size and the thermal properties of the sediment, and is typically on the order of 40-80 m a$^{-1}$ (Zoet & Iverson, 2020).

#### *3.1.3 Heave and supercooling*

The final term for equation (2) is the vertical heave force, $V$, which depends on the thermal properties of the ice and sediment within the fringe (Rempel, 2008; Meyer et al., 2019, 2021). Critically for both frozen fringe evolution and thermal regelation, the base of the fringe is warmer than the top of the fringe, leading to a negative thermal gradient $G$ in the vertical, defined by (Meyer et al., 2019):

$$G = -\frac{Q_g + u_b \tau_b}{K}, \tag{5}$$

where $K$ is the thermal conductivity, and the other terms follow from equation (3). If we assume that the temperature distribution through the fringe is approximately linear, we can define a non-dimensional parameter, $\theta$, for the amount of supercooling at the top of the fringe:

$$\theta = 1 - \frac{G H_f}{T_m - T_f}, \tag{6}$$

where $T_m$ is the bulk melting temperature of ice, and $T_f$ is the temperature at the base of the fringe, governed by the critical effective pressure $N_0$ and the bulk thermal properties of ice (Meyer et al., 2019). Then, the heave rate is a nonlinear function of both

$N$ and $\theta$:

$$V = V_0 \frac{V_1(\theta, \phi) - \frac{N}{N_0}}{V_2(\theta, \phi) + \Pi}, \tag{7}$$

where $V_0$ is the nominal heave rate, $V_1$ and $V_2$ are functions of supercooling $\theta$ and porosity $\phi$ alone, and $\Pi$ can be thought of as a flow resistance parameter (Meyer et al., 2019).

To summarize, frozen fringe growth begins when ice rests on an unlithified bed under high effective pressure. The fringe grows in thickness as pressure and premelting drive infiltration of the ice into the sediment layer, and decreases in thickness as basal melt releases material below the fringe. Because the sliding interface sits beneath the fringe, the entire package is advected in the direction of ice flow.

### 3.2 Thermal regelation

In any glacier with temperate ice near the base, supercooling at the top of the frozen fringe will create a positive thermal gradient in the few meters of ice above it. Distinct from pressure regelation (Iverson, 1993; Iverson & Semmens, 1995), in which ice melts and refreezes around clasts, thermal regelation is the process by which sediment will migrate towards warmer ice, as either individual clasts or small clusters of fine particles (Nye, 1967; Gilpin, 1979; Wettlaufer & Worster, 2006). Sediment grains within the ice matrix will form micron-scale premelted films of water around them, which give rise to disjoining forces around the particle. On the cold side of the particle or cluster, where the film is thinner, there is a greater disjoining force, thus driving the sediment along the thermal gradient.

From the frozen fringe model described above, we can use the supercooling parameter $\theta$ to model the temperature gradient above the fringe. The temperature at the top of the fringe $T_l$ is given by:

$$T_l = T_m - \theta(T_m - T_f). \tag{8}$$

The thermal gradient through the ice above the fringe, $G_i$, is either set by the gradient created by premelting and refreezing within the frozen fringe, $G_f$, or the gradient caused by changes in the pressure-melting-point of ice with depth, $G_p$. Altogether, this gives:

$$G_i = max[G_p, G_f], \tag{9}$$

for

$$G_p = \beta \rho_i g, \tag{10}$$

where $\beta$ is the Clapeyron slope for ice, and for

$$G_f = \frac{T_m - T_l}{z_0}, \tag{11}$$

where $z_0$ represents a critical height above the frozen fringe where the supercooling signal has been diffused away. Without employing a full thermal model for the three-dimensional energy balance within the glacier, we have very few constraints on $z_0$. However, thermal regelation ceases when particles reach the isotherm $T = T_m$ (You et al., 2021), and we readily observe particles transported by regelation to several meters within the ice mass, indicating that $z_0$ should be on the order of meters, at minimum.

Once we have modeled the thermal gradient above the fringe, the maximum vertical velocity for particles and clusters undergoing regelation, which we denote as $R_s$, is given by:

$$R_s = \frac{3\Gamma K}{1 + \Gamma \rho_i L} G_i, \tag{12}$$

where $\Gamma$ is a constant function of the thermal properties of ice and sediment (You et al., 2021). In this formulation, the vertical velocity of particles above the fringe scales linearly with the amount of supercooling above the fringe, which itself is a function of fringe thickness. In this way, the evolution of a solid cryofacies during frozen fringe formation also drives the growth of an overlying dispersed cryofacies via thermal regelation.

| Variable | Notation | Default value | Units | Sensitivity range |
|---|---|---|---|---|
| Thickness of frozen fringe | $H_f$ | | m | |
| Thickness of dispersed layer | $H_d$ | | m | |
| Effective pressure | $N$ | $10^5$ | Pa | $[10^4, 5 \times 10^5$ |
| Sliding velocity | $u_b$ | $1.58 \times 10^{-6}$ | m s$^{-1}$ | $[1.58 \times 10^{-7}, 3.17 \times 10^{-5}]$ |
| Basal shear stress | $\tau_b$ | $56.3 \times 10^3$ | Pa | $[50 \times 10^3, 100 \times 10^3]$ |
| Geothermal heat flux | $Q_g$ | 0.06 | W m$^{-2}$ | $[0.02, 0.1]$ |
| Till grain radius | $r$ | $4 \times 10^{-5}$ | m | $[5 \times 10^{-6}, 5 \times 10^{-4}]$ |
| Pore throat radius | $r_c$ | $10^{-6}$ | m | $[10^{-5}, 10^{-7}]$ |
| Critical depth | $z_0$ | 10 | m | $[5, 100]$ |
| Cluster volume fraction | $f_c$ | 0.64 | None | $[0.3, 0.9]$ |
| Till friction angle | $\varphi$ | 32 | $^\circ$ | $[15, 40]$ |
| Sediment thermal conductivity | $k_s$ | 6.27 | W m$^{-1}$ K$^{-1}$ | $[0.5, 8.5]$ |
| Frozen fringe porosity | $\phi$ | 0.4 | None | $[0.25, 0.45]$ |
| Frozen fringe permeability | $k_0$ | $4.1 \times 10^{-17}$ | m$^2$ s$^{-1}$ | $[10^{-18}, 10^{-16}]$ |
| Surface energy | $\gamma$ | $3.4 \times 10^{-2}$ | J m$^{-2}$ | |
| Critical pressure | $N_0$ | Eq. (1) | Pa | |
| Basal melt rate | $m_b$ | Eq. (2) | m s$^{-1}$ | |
| Heave rate | $V$ | Eq. (7) | m s$^{-1}$ | |
| Fringe saturation | $\bar{S}$ | (Meyer et al., 2019), Eq. (7) | None | |
| Ice density | $\rho_i$ | 917 | kg m$^{-3}$ | |
| Latent heat of ice | $L$ | $3.34 \times 10^5$ | J kg$^{-1}$ | |
| Threshold velocity | $u_t$ | (Zoet & Iverson, 2020), Eq. (2) | m s$^{-1}$ | |
| Basal slip exponent | $p$ | 5 | None | |
| Temperature gradient | $G$ | Eq. (5) | K m$-1$ | |
| Ice thermal conductivity | $K$ | 2 | W m$^{-1}$ K$^{-1}$ | |
| Supercooling | $\theta$ | Eq. (6) | None | |
| Ice melting temperature | $T_m$ | 273 | K | |
| Fringe base temperature | $T_f$ | (Meyer et al., 2019), Eq. (6) | K | |
| Fringe upper temperature | $T_l$ | Eq. (8) | K | |
| Fringe resistance | $\Pi$ | (Meyer et al., 2019), Eq. (14b) | Pa m$^{-1}$ s$^{-1}$ | |
| Heave components | $V_0$, $V_1$, $V_2$ | (Meyer et al., 2019), Eq. (13) | | |
| Ice Clapeyron slope | $\beta$ | $7.2 \times 10^{-8}$ | K Pa$^{-1}$ | |
| Gravitational acceleration | $g$ | 9.81 | m s$^{-1}$ | |
| Regelation rate | $R_s$ | Eq. (12) | m s$^{-1}$ | |
| Regelation coefficient | $\Gamma$ | (You et al., 2021), Eq. (8) | None | |

**Table 1.** Notation, default values, and ranges for model variables. Where default values include references, the equation number denotes an equation in the referenced work.

### 3.3 Governing equations

In this simplified form, both the frozen fringe and thermal regelation models track moving interfaces within an ice column. However, to accurately predict sediment transfer beneath a flowing glacier or ice sheet, we need to account for the lateral movement of material. Because ice is incompressible to a first-order approximation, the advection of an ice column may further extend or compress the layers when the velocity profile diverges or converges, respectively. To capture these effects, we implement general advection equations for the source terms for the frozen fringe thickness $H_f$, and the dispersed layer thickness $H_d$, from (2) and (12), respectively:

$$\frac{\partial H_f}{\partial t} + u_b \cdot \nabla H_f + H_f \nabla \cdot u_b = \frac{-m - V}{\phi \bar{S}}; \tag{13}$$

$$\frac{\partial H_d}{\partial t} + u_b \cdot \nabla H_d + H_d \nabla \cdot u_b = R_s; \tag{14}$$

where $u_b$ represents the *horizontal* components of ice sliding velocity (e.g., x- and y-directed velocities in a Cartesian frame), and we have neglected to account for the minimal reduction in fringe thickness caused by transferring individual particles into the overlying dispersed layer. The first term in each equation represents the change in thickness of each respective layer, the second term treats the advection of layers with the ice flow, the third term handles the thickening or thinning of layers as ice diverges or converges, and the right-hand side of each equation governs the growth or decay of each layer due to entrainment or deposition of sediment.

## 4 Numerical implementation

### 4.1 Sensitivity to key variables

To assess the relative importance of different input variables in the basal sediment entrainment model, we run a series of numerical experiments over idealized 1D ice columns. In each model run, we only consider vertical sediment entrainment and redistribution between the fringe and dispersed layers. We test variables individually, holding other parameters fixed (Table 1). Each simulation runs for 250 years (a typical advection time scale for a parcel of ice to travel from the ice divide to the terminus (Motyka et al., 2003; A. Gardner et al., 2022; Porter et al., 2022)). In each experiment, the frozen fringe equilibrates to its final thickness within 25 years or less; this thickness value then defines the growth rate for the dispersed layer. As such, the choice of time scale matters quantitatively, but should not change the qualitative sensitivity results. Lastly, we allow an infinite sediment supply beneath the idealized ice column, and ignore any effects from the lateral advection of ice and sediment.

### 4.2 Coupling with IGM

To run full two-dimensional simulations of sediment entrainment, deformation, and transport to the glacier terminus, our modeling framework requires a realistic quantification of the ice sliding velocity field. Here, we use the Instructed Glacier Model (IGM) to generate boundary conditions for Mendenhall Glacier (Jouvet & Cordonnier, 2023). IGM leverages a physics-informed convolutional neural network (CNN) (Raissi et al., 2019), trained to minimize the energy associated with the Glen-Stokes equations for ice flow (Kharazmi et al., 2019), to approximate a solution for the dynamic evolution of a given glacier. Compared to traditional high-order ice flow models, IGM improves computational performance by multiple orders of magnitude over large domains (the size of a glacier or icefield) with minor sacrifices in terms of accuracy. IGM has extensively been tested against well-constrained alpine glacier dynamics in the Alps (Jouvet et al., 2022). We use the data assimilation module within IGM to employ observations of glacier geometry and surface velocity and predict a plausible sliding velocity field (Jouvet, 2023). This

module is well-suited to solving the underlying optimization problem as CNNs easily allow for automatic differentation (Baydin et al., 2018).

To generate realistic sliding velocity fields for Mendenhall Glacier's present-day geometry, we run the $O_{-d}$ optimization scheme presented in (Jouvet, 2023). For this scheme, we use an interpolated ice thickness field from the Ice Thickness Model Intercomparison eXperiment (ITMIX) (Farinotti et al., 2019, 2021) and surface velocities from the ITS_LIVE project from NASA MEaSUREs (A. Gardner et al., 2022). The optimization algorithm searches for distributed ice thicknesses and ice flow parameters that yield the best fit between modeled variables and the observed variables listed above, while minimizing the misfit to the Glen-Stokes equations (i.e., minimizing free energy).

Resolving the sliding behavior of a glacier from observed variables at its surface is an under-determined problem. If an inverse solver under-estimates the glacier's surface velocity, for example, that discrepancy might be accommodated by: increasing ice thickness, increasing ice fluidity, decreasing basal friction (through any combination of material properties of the bed, subglacial hydrology, thermal regime, and so forth), increasing bed slope, or any (likely non-linear) combination of the above. Given our incomplete understanding of basal processes (Zoet et al., 2021; Gilbert et al., 2022; Hoffman et al., 2022; Köpfli et al., 2022; Woodard et al., 2023), most inversion schemes, including IGM, use (one or more) dimensionless, non-physical sliding coefficient(s) to approximate the combined effects of hydrology, basal friction, thermal regime, and other non-geometric controls on sliding behavior. Here, we leverage the process-agnostic behavior of IGM to produce multiple realistic scenarios for Mendenhall Glacier's sliding behavior through adapting this dimensionless sliding coefficient. In doing so, IGM identifies two sliding regimes that best fit the input data: (1) a `SLOW` scenario with less slip at the bed and a thicker glacier, and (2) a `FAST` scenario with generally higher sliding velocity and lower ice thickness.

### 4.3 Advection scenarios

To investigate the effects of deformation and advection on sediment transport to the terminus, we run eight different 2D simulations over a range of effective pressure scenarios, ranging from 40% to 5% of overburden pressure. At Mendenhall Glacier, it takes any given parcel of ice anywhere between 250-350 years to travel along the main stem, from the ice divide to the terminus, such that the sediment entrainment model must run for at least that period across the entire extent of the glacier. Rather than incorporating a process model of subglacial hydrology, which may need to run on hourly or sub-hourly time scales and introduces additional unconstrained parameters (Werder et al., 2013; Sommers et al., 2018; Delaney et al., 2019), we instead consider the long-term, mean effective pressure at each grid cell. In general, basal water pressure will be related to the overburden pressure of the ice, with different scalings based on the configuration of the hydrologic system (Arnold & Sharp, 1992, 2002; Flowers, 2015). Where water is transported efficiently through channels in the ice or sediment, basal water pressure tends to be lower; conversely, if water is transported inefficiently through sheets, cavities, and/or porous flow, basal water pressure will be greater (Flowers, 2015). A common scaling relationship holds that grid cells with channelized features will have long-term, mean water pressure around 60-80% of overburden, while cells with cavity features will have long-term, mean water pressures around 90-95% of overburden (Arnold & Sharp, 1992, 2002; Flowers, 2015). As such, rather than explicitly simulate Mendenhall Glacier's hydrology, we scale the effective pressure to a value between 40% and 5% of overburden pressure, in order to remain agnostic to any choice of specific hydrologic configuration. While these experiments keep the sliding velocity and effective pressure fields constant in time, we note that equations (13) and (14) are fully general, such that explicit process models of glacier sliding and hydrology could be fully integrated into the coupled model at each time step.

For each of our sixteen advection experiments (two sliding scenarios times eight pressure scenarios), we set all other parameters to their default values from Table 1, informed by qualitative field observations at Mendenhall Glacier and laboratory experiments (Rempel, 2008; Meyer et al., 2019; You et al., 2021). Figure 3b provides an overview of our complete coupled model framework, from input variables, to boundary condition generation with IGM, through multiple model scenarios, to a final estimate of sediment fluxes. To solve the advection-reaction equations (13) and (14), we employ a total-variation-diminishing (TVD) algorithm using a finite volume discretization on a regular grid in the Landlab modeling framework (Barnhart et al., 2020). We set the till layer to a large initial value (10 m) everywhere beneath the glacier, such that sediment supply does not limit the entrainment model. While this may be over-exaggarated, a thick till layer is thought to be present under Mendenhall Glacier and many other Alaskan tidewater glaciers. Before introducing advection, we spin-up an initial frozen fringe and dispersed layer over 25 years, with time steps systematically increasing from $10^{-2}$ to $6.3{\times}10^{4}$ seconds. We then run the coupled model for 300 years, with time steps of $10^{6}$ seconds (11.57 days). At each step, we calculate the sediment flux at the terminus by multiplying the thickness of the debris-rich layers by the grid spacing, the sliding velocity, and the sediment concentration of each layer. To avoid boundary artifacts at the edge of the domain, we integrate sediment fluxes over the last two grid cells nearest the terminus, given that ablation, calving, mass wasting, and other geomorphic processes will act to remove sediment once it has reached the end of the glaciated domain.

## 5 Sensitivity experiments

Figure 4 presents the results from sensitivity experiments for 12 key variables of interest. Effective pressure is the most impactful variable governing sediment fluxes delivered by the frozen fringe, especially in the 80-200 kPa range typical of alpine glaciers. Conversely, the flux from the dispersed layer depends more strongly on sliding velocity than effective pressure, as the layer is insulated from basal melt by the fringe below it, and thus sliding velocity scales the delivery of sediment without the counterbalancing effect of removing entrained material. The sediment flux from the fringe also increases with sliding velocity up until approximately 200 m $a^{-1}$. At this threshold, the effects of frictional heating begin to dominate the rate balance of fringe growth and transport. While lower in magnitude than effective pressure and sliding velocity, basal shear stress and geothermal heat flux have a negative relationship with fringe thickness, as expected, since these variables play a strong role in determining the basal melt rate. In cold-based glaciers, negative basal melt rates, corresponding to net freeze-on, would have the opposite effect of increasing the fringe thickness and the overall sediment flux.

The middle and bottom rows of Figure 4 explore the properties of the source sediment till package. In general, entrainment in the frozen fringe is more efficient for smaller sediment grain sizes, and may shut down entirely for clasts that are mm-scale or larger (coarse sand). In field observations, however, we do find large grains entrained in the frozen fringe and higher in the ice column, so it is likely that these particles become entrained as part of an overall poorly sorted sediment layer and not as isolated clasts. Pore throat radius beneath the frozen fringe is traditionally taken to equal 1 $\mu m$ (Meyer et al., 2019), but we note that any coupling between grain size and pore throat radius will increase the effect of the negative relationship shown here. We find that the till friction angle, a metric of shear strength, is also an important control on fringe growth, as it exerts a positive control on the shear stress from a deforming bed (Zoet & Iverson, 2020). The thermal conductivity and permeability of the sediment, assuming poor sorting characteristic of glacial tills, increases the infiltration rate of the fringe, leading to thicker fringe layers. In contrast, as the porosity of the till layer increases (in the absence of an associated increase in permeability), the overall sediment flux decreases, as more of the total volume of the fringe layer is composed of ice and liquid water.

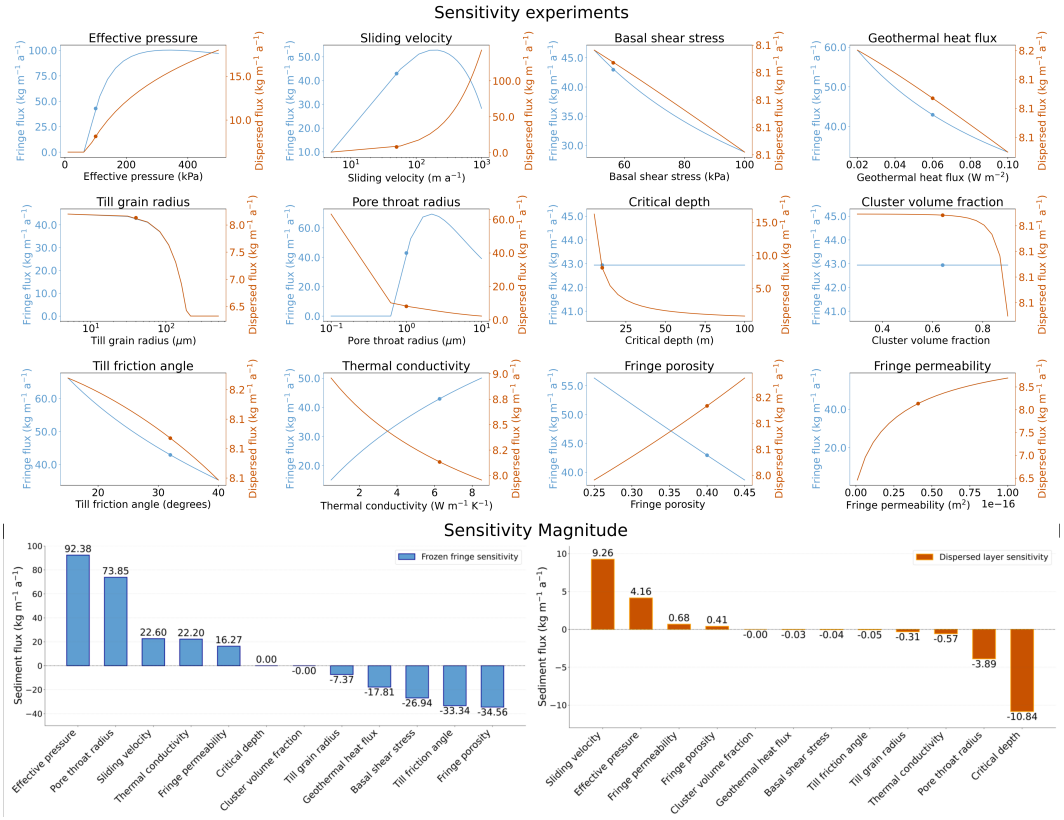


**Figure 4.** Results from 1D column sensitivity experiments for 12 variables of interest (Table 1). Variables were tested by stepping through a range of values (shown on each x-axis), while holding each other parameter at a default value (shown as points on each plot). Default values were chosen from literature values for frozen fringe physics (Rempel, 2008; Meyer et al., 2019) and alpine glacier mechanics (Cuffey & Paterson, 2010). Note the change in y-axis scales between subplots. The two lowest panels show the sensitivity of sediment fluxes from the frozen fringe (blue, left) and dispersed layer (orange, right) for each variable at its default value.

Few of the other sediment property parameters change the behavior of the dispersed layer in isolation, except for the critical depth - the height above the frozen fringe where thermal regelation shuts down. While it is difficult to constrain this parameter without detailed temperature measurements from within basal ice layers, we note that it should be on the order of several meters or more to allow for meters-thick debris layers to form. A conservative estimate could take a critical depth equal to the entire thickness of the glacier, at which point the model proves much less sensitive to marginal changes in this parameter. The cluster volume fraction, representing the volume of clustered particles occupied by sediment rather than saturated pore space, alters the regelation rate of these clusters within the dispersed layer (You et al., 2021). However, it has little influence over the growth rates until the clusters are 80% sediment or more, which is very unlikely to occur in reality.

# 6 Advection experiments

## 6.1 Results from inverse modeling

After investigating the sensitivity of the model in a one-dimensional framework, we turn to two-dimensional, plan-view models to assess the spatial variability of entrainment and sediment transport at Mendenhall Glacier. First, we use an inverse method with IGM's data assimilation module to infer the glacier's sliding velocity field given remote sensing observations of topography, ice thickness, and surface velocities. After exploring a range of configurations for the optimization scheme, Figure 5 shows the inferred ice thickness and sliding velocity fields for the two best-fitting scenarios, which we term `FAST` (Fig. 5, upper row) and `SLOW` (Fig. 5, lower row), based on the mean magnitude of sliding velocity in the glacier's main stem. All inversion parameters were held constant between the two scenarios, with the exception of the initial value of the sliding coefficient, which was 35 km $\mathrm{MPa}^{-3}$ $\mathrm{a}^{-1}$ and 15 km $\mathrm{MPa}^{-3}$ $\mathrm{a}^{-1}$, respectively. In each case, the loss function converged to within 1% of its final value in the first 200 iterations (of a total of 500 iterations) of the optimization scheme, such that we can be reasonably confident that the fit to observations would not be improved by further iteration. Standard deviations between inferred (optimized) and observed (input) values are reported in each figure, ranging from 54.59 - 62.06 m in ice thickness, and from 9.99 - 11.01 m $\mathrm{a}^{-1}$ in *surface* velocity (as we do not have independent measurements of sliding velocity at this site). From the results of the ITMIX project, we might expect deviations in ice thickness of at least 16% (ensemble median) and ideally not greater than 31% (75th percentile), given the lack of measured ice thickness profiles at Mendenhall Glacier (Farinotti et al., 2021). Here, the misfit between our modeled ice thickness profiles and the ITMIX ensemble is well within the expected uncertainty range at 10-12% of the maximum ice thickness. Uncertainty in surface velocities from ITS_LIVE are within 0.1 - 4.5 m $\mathrm{a}^{-1}$ at Mendenhall Glacier (A. S. Gardner et al., 2018; A. Gardner et al., 2022), less than half that of our reported misfit.

Overall, the observed ice thickness and sliding velocity profiles fit the range of behavior we might expect from a typical alpine glacier. In both scenarios, Mendenhall Glacier reaches a maximum ice thickness in the main stem of 500-550 m, a roughly 10-20% decrease in thickness since the last published radar measurements from 2002 (Motyka et al., 2003). Upstream from the main stem, the north and south branches of the glacier are thinner than expected in both scenarios, achieving thicknesses of only 300-400 m. At the terminus, the inferred ice thickness is between 25 and 50 m, consistent with observed rates of thinning since the early 2000's (Motyka et al., 2003). Figure 6 shows the resulting effective pressure distributions for both scenarios for a range of different effective pressure scalings discussed previously. As expected, the `SLOW` configuration yields greater maximum pressures, and the vast majority of grid cells in each scenario will have enough pressure to begin forming a frozen fringe.

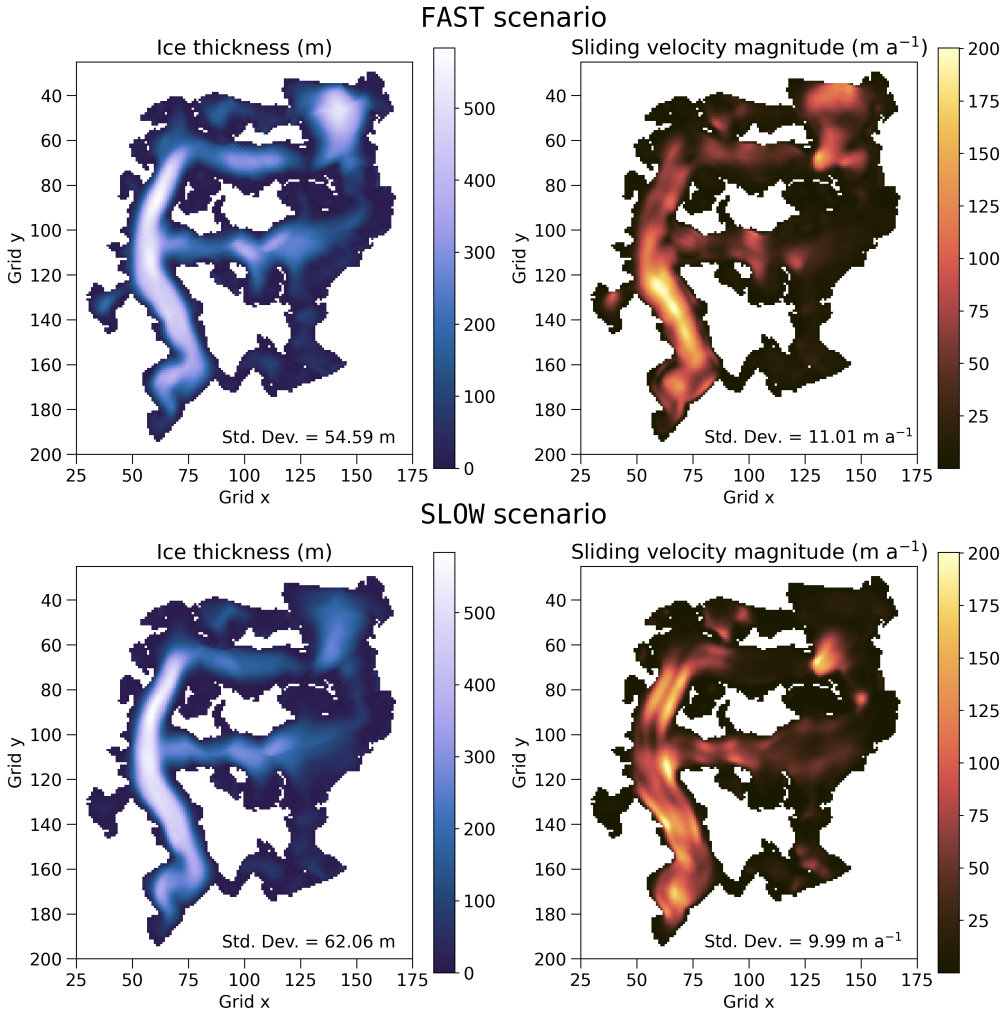


**Figure 5.** Results from the inverse method, using IGM's data assimilation module to produce two realistic model scenarios for ice thickness and sliding velocity at Mendenhall Glacier. The `FAST` scenario is shown in the top row, with the `SLOW` scenario in the bottom row. Standard deviations are reported in each figure, for inferred-observed ice thickness and inferred-observed *surface* velocity, respectively.

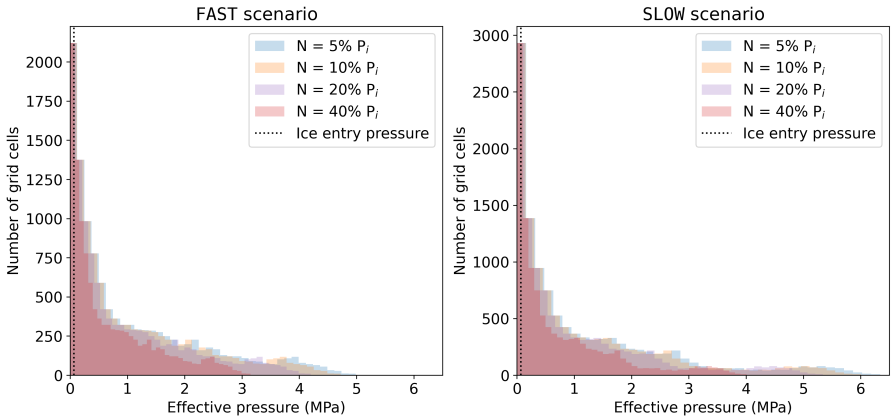


**Figure 6.** Histograms of effective pressure given the inferred ice thicknesses from the optimization scheme for the `FAST` (left) and `SLOW` (right) sliding scenarios. Effective pressures are plotted for four of the eight pressure scalings, to ease interpretation, with a vertical dotted line marking the pressure at which ice can begin infiltrating the underlying sediment matrix.

Estimated sliding velocities in both scenarios reach a maximum of nearly 180 m $a^{-1}$, but exhibit markedly different spatial patterns. Stake measurements in the previously discussed 2002 campaign showed maximum ice velocities of 145-172 m $a^{-1}$, near-terminus velocities of 51-81 m $a^{-1}$, and velocities in the upper reach of 34-153 m $a^{-1}$ (Motyka et al., 2003). As such, the magnitude of our inferred velocity profiles would be consistent with acceleration in the main stem and terminus around 20 m $a^{-1}$, and rapid deceleration consistent with thinner ice profiles in the upper reaches of the north and south stems. At the upper icefall (grid coordinates [135, 70] in Figure 5), we infer sliding velocities of 150-175 m $a^{-1}$, concurrent with a drop in surface elevation of several hundreds of meters over a similar along-flow distance. Between the two scenarios, the `FAST` sliding velocity profile reaches its maximum after the junction between the two branches, south of the Mendenhall Towers, and maintains that elevated sliding velocity profile until the last 1-2 km before the terminus. Conversely, the `SLOW` scenario exhibits a more consistent velocity along the entirety of the glacier's main stem, but shows a deeper trough along the center of the glacier where deformation comprises a larger proportion of the total velocity. The region where sliding dominates is wider, filling most of the main stem, but less homogeneous, with patches of slower motion interspersed along the flow. Finally, we note that mean absolute error in the assimilated surface elevation was less than 1 m in both scenarios, and the ice mask was fit well within our grid tolerance.

### 6.2 Sediment flux results

Figure 7 presents the steady-state frozen fringe thicknesses from four example model runs. Generally, we see that the spatial extent of frozen fringe beneath the glacier is largely determined by the effective pressure scaling. When the effective pressure is 10% of overburden pressure or less, no frozen fringe survives to, nor forms at, the glacier terminus. Overall, the size of the frozen fringe responds to changes in both effective pressure and sliding velocity, with higher pressures and slower velocities leading to greater layer thicknesses. In the `SLOW` scenario, with effective pressure scaled to 40% of overburden, the frozen fringe reaches a maximum of 5 m, concentrated in the upper, stagnant reaches, near the slow-moving margins, and near the terminus where the flow field converges. As effective pressure decreases, the maximum fringe thickness in the same regions decreases to 2.5 m. While the spatial pattern of fringe thickness is similar, qualitatively, in the `FAST` sce-

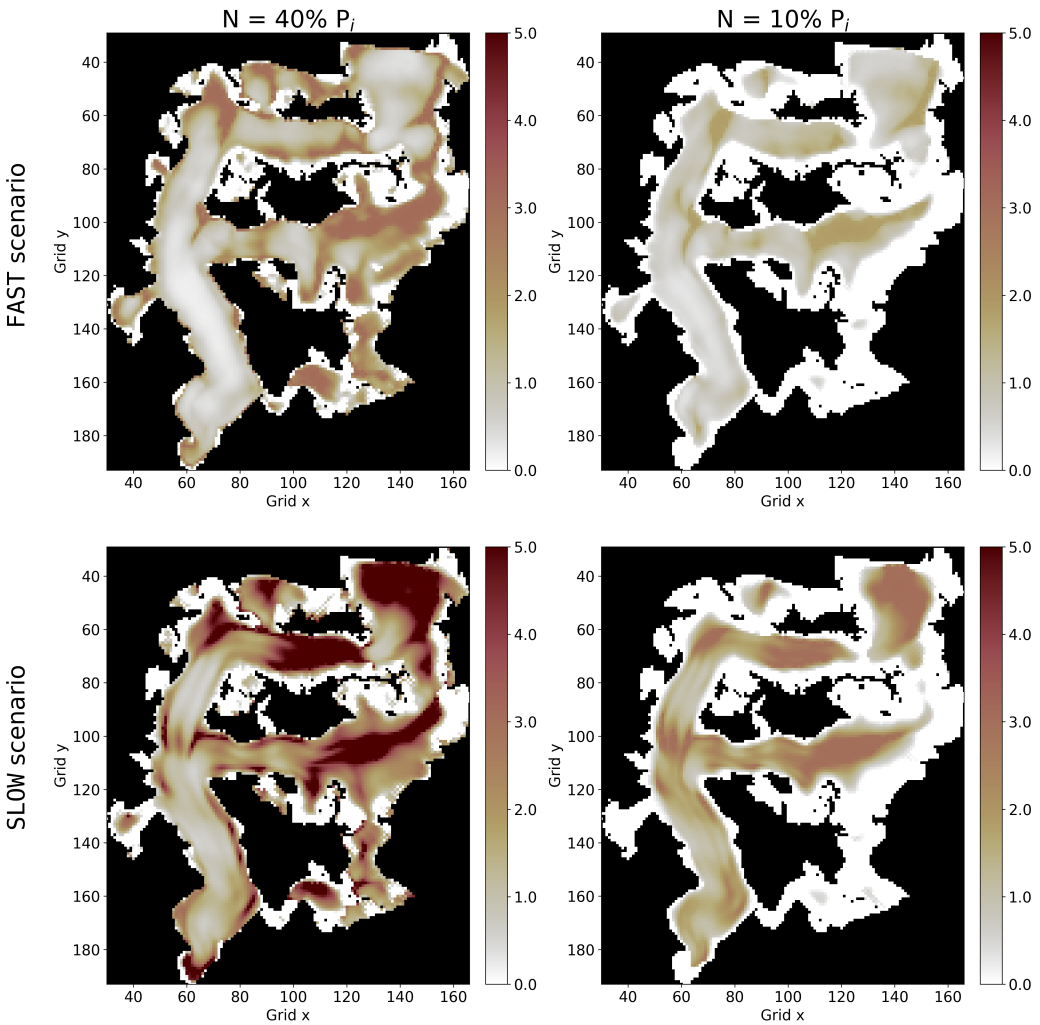


**Figure 7.** Modeled steady-state frozen fringe thickness across the extent of Mendenhall Glacier. Plots are arranged by sliding scenario (rows) and pressure scenario (columns) for four example model runs.

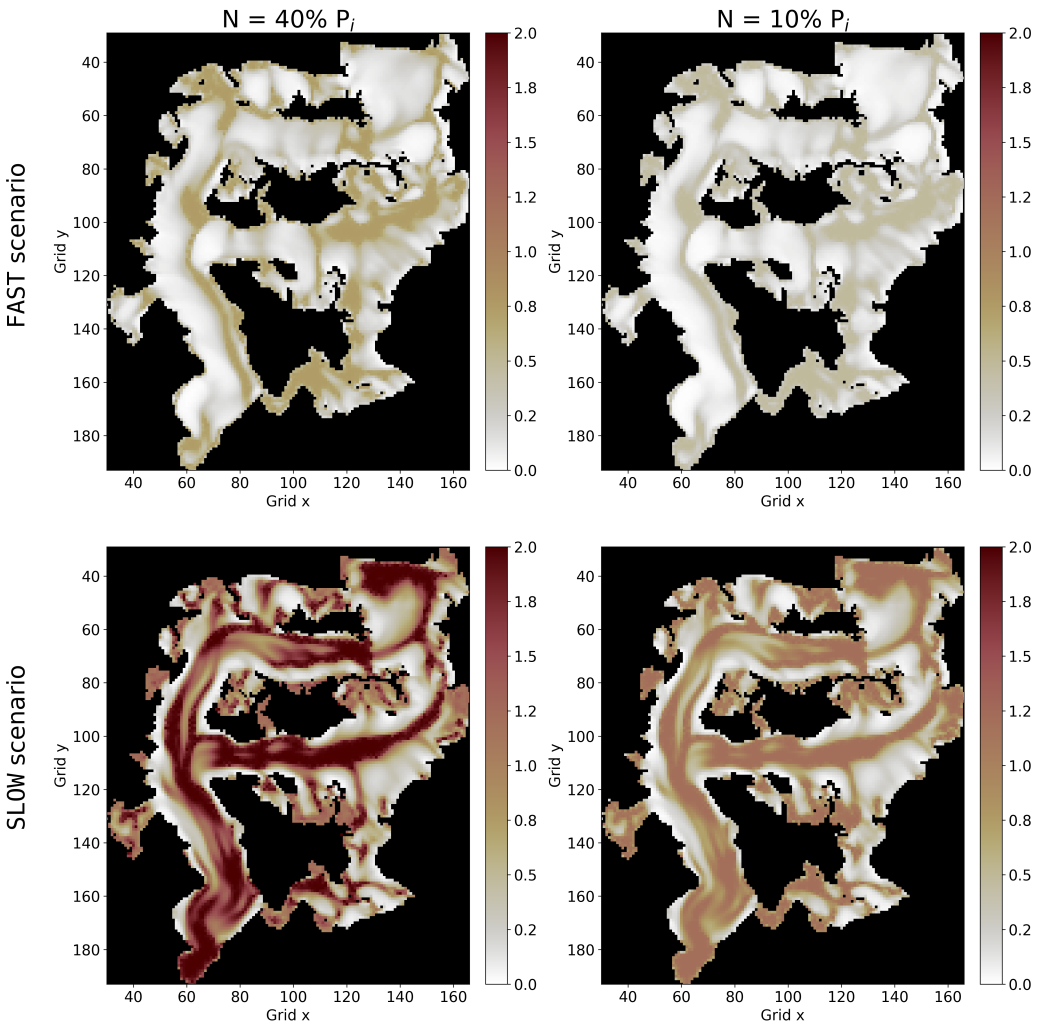


**Figure 8.** Modeled dispersed layer thicknesses across the extent of Mendenhall Glacier, shown after 300 years of simulated time. Plots are arranged by sliding scenario (rows) and pressure scenario (columns) for four example model runs.

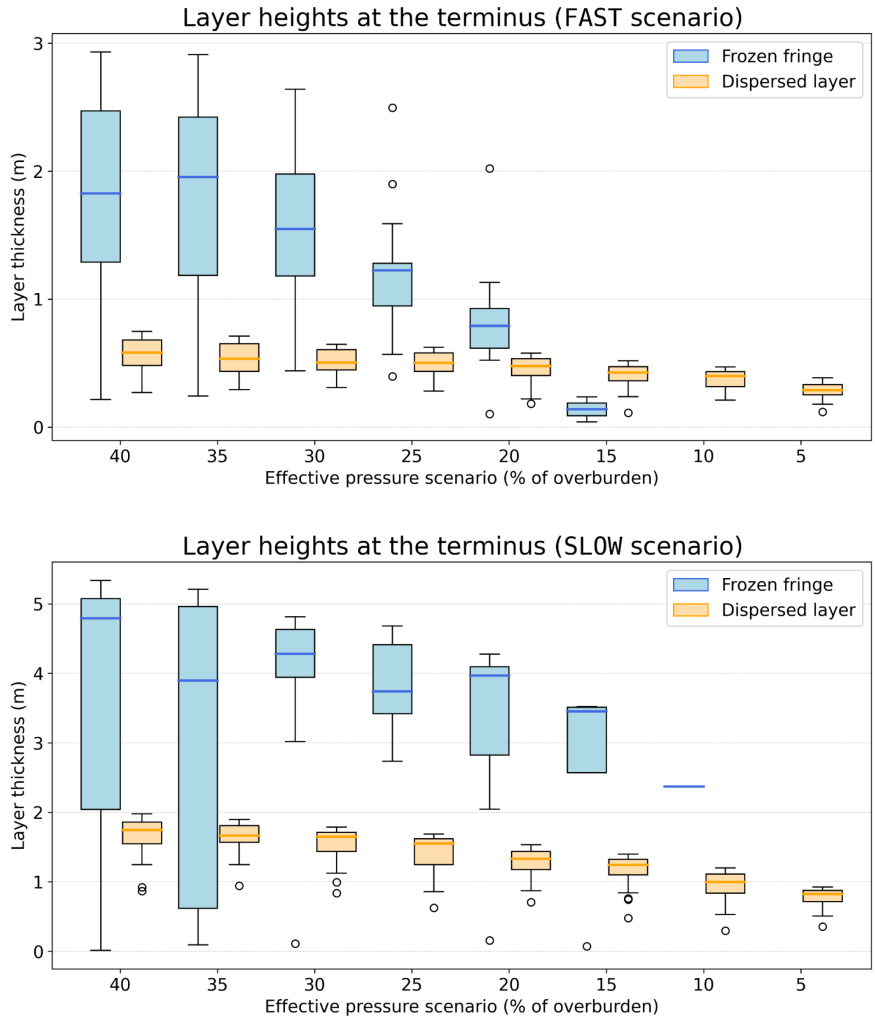


**Figure 9.** Modeled layer thicknesses within two grid cells of the glacier terminus for the frozen fringe (blue) and dispersed layer (orange) across all of the model scenarios. Median values are shown in bold, horizontal lines, with outliers denoted by open circles. Note that across both the `FAST` and `SLOW` scenarios, no frozen fringe survives to the terminus when effective pressure is 10% or less of overburden pressure (cf. Fig 7).

nario, the maximum fringe thickness ranges from 3 m to 1.25 m across the effective pressure scenarios.

Similarly, Figure 8 presents the dispersed layer thicknesses after 300 years of simulated entrainment, deformation, and advection. In every scenario, the dispersed layer reaches the glacier terminus, insulated from basal melt by the presence of underlying frozen fringe. In the `SLOW` scenarios, the dispersed layer ranges from 0.8 - 1.8 m in thickness, with the largest layers forming under regions with thick ice, and thus relatively higher pressures. In the `FAST` scenarios, the dispersed layer never increases beyond 0.2 - 0.6 m in thickness, and becomes concentrated along the margin of the main stem as it is advected by the ice flow. The spatial pattern of dispersed layer thicknesses remains constant as the effective pressure varies, only altering in magnitude with each successive scaling scenario.

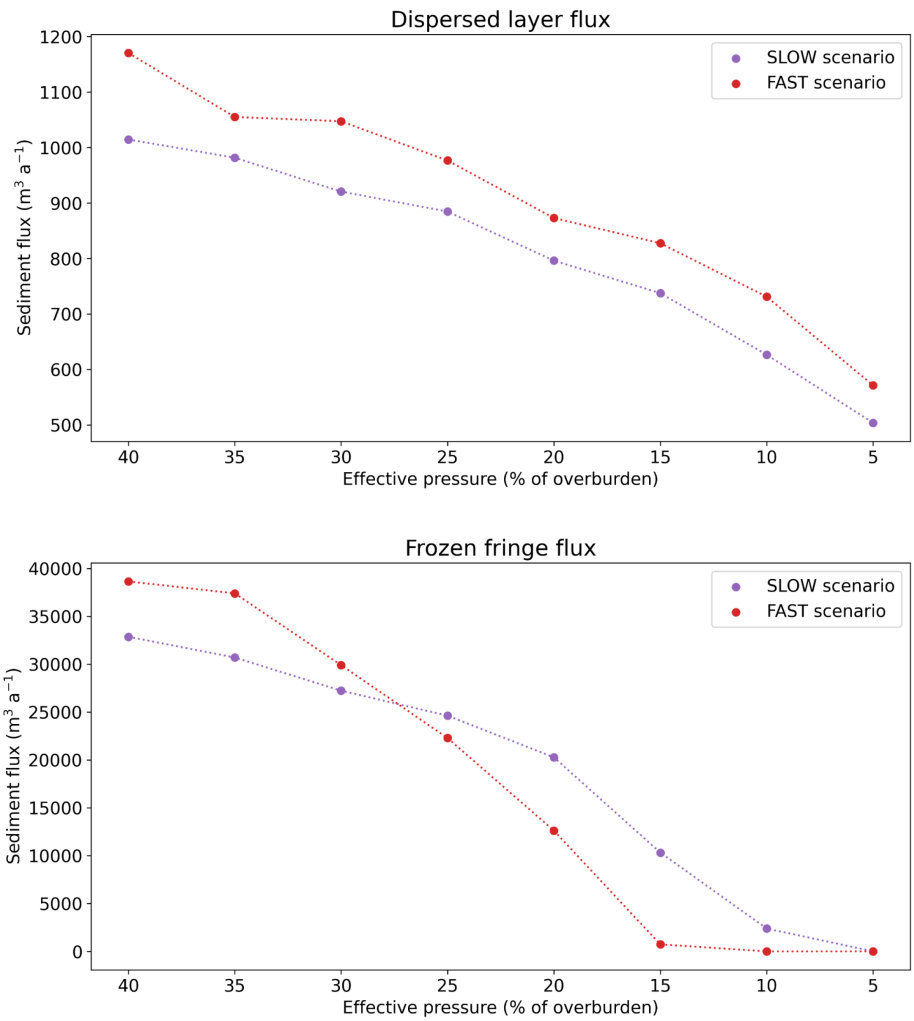


**Figure 10.** Entrained sediment fluxes from each model scenario, partitioned by source layer, with the dispersed layer plotted above the frozen fringe. Note that the y-axis scale changes by over an order of magnitude between the two plots.

While our models consider the advection of sediment along the entire flow path of the glacier, field observations are limited to easily-accessible outcrops of ice near the terminus. To compare with our observations, Figure 9 aggregates the layer thicknesses in the two grid cells nearest the terminus for each scenario. We see that the median frozen fringe at the terminus ranges from 0 - 1.8 m thick in the `FAST` scenarios, and 0 - 4.9 m in the `SLOW` scenarios. In both suites, frozen fringe does not begin to reach the terminus until effective pressure is greater than 10% of overburden, and remains sparse, spatially, until effective pressure is 20% of overburden. The dispersed layer demonstrates much less variability between scenarios, but the overall magnitude is approximately 1 m greater in the `SLOW` suite than the `FAST` suite. Of note, both frozen fringe and dispersed layer thicknesses display a sub-linear scaling with effective pressure, increasing less rapidly at high effective pressures than at pressures around 10-20% of overburden.

Given the inferred sliding velocities from IGM, modeled thicknesses of debris-rich sediment layers, and the concentrations of sediment in each layer obtained from literature (frozen fringe, (Meyer et al., 2019)) and field measurements (dispersed), we estimate the sediment flux contribution from each stratigraphic unit. Figure 10 shows the results, partitioned between layers. The maximum flux from the frozen fringe is 32,860-38,640 $m^3$ $a^{-1}$, and the maximum flux from the dispersed layer is 1,014-1,170 $m^3$ $a^{-1}$. The dispersed layer fluxes increase monotonically as pressure increases, and the fluxes from the `FAST` scenario are always greater than the fluxes from the `SLOW` scenario for a given pressure scaling. The frozen fringe displays more nonlinearity: when effective pressure is scaled to 25% of overburden pressure or less, the `SLOW` scenarios transport more sediment in the frozen fringe than the `FAST` scenarios; this trend is reversed for effective pressures above 25% of ice pressure. Across all model realizations where both units were present at the terminus, the flux from the dispersed layer was between 3 - 6% of the flux from the frozen fringe.

## 7 Discussion

We show that sequences of solid and dispersed basal ice facies may be explained by frozen fringe evolution and thermal regelation. We suggest a new mechanism for dispersed facies formation: (1) as a frozen fringe initiates beneath an ice mass, there is a slight depression in ice temperature at the top of the fringe, (2) leading to a temperature gradient from colder to warmer ice in the region above the fringe, (3) which allows individual sediment grains and clusters of grains to travel via thermal regelation into the layer above the frozen fringe. We present governing equations for the evolution of coupled frozen fringe and dispersed sediment layers, composing a process model that is readily coupled with existing models of glacial landscape evolution.

We note that our approach has several limitations. Both processes in this model (frozen fringe evolution and thermal regelation) are supported by theory and laboratory experiments (Wettlaufer & Worster, 2006; Rempel, 2008; Meyer et al., 2021; You et al., 2021), but we do not have any experimental controls at the spatial (O[$10^3$]-[$10^4$] $m^2$) or temporal (O[$10^2$] years) scales of alpine glacier dynamics. Because we do not explicitly simulate the temperature and enthalpy distribution within the ice column (e.g., (Aschwanden et al., 2012; Hewitt & Schoof, 2017)), we are implicitly assuming that the entire glacier is temperate, with the vertical temperature profile set by the change in pressure-melting point throughout the ice column. While most other heat sources (e.g., strain heating) will be accommodated by changes in ice porosity and water content in a temperate glacier (Hewitt & Schoof, 2017), our current model is not suitable for polythermal ice masses. Further, we do not use any external constraints on erosion rates or fluvial sediment transport in this work. If the sedimentary system beneath Mendenhall Glacier is transport-limited, our predictions of glacial sediment fluxes may be reasonable, as the features of the subglacial hydrologic system are likely to not be as spatially widespread as the frozen fringe. We have made the assumption throughout this work that the glacier is under-

lain by unlithified material, forming a soft, deformable bed, and presenting a ready supply of sediment for basal entrainment. This assumption is reasonable where glaciers flow over easily erodible lithologies or previous till deposits, such as at Mendenhall Glacier, but do not hold where the bedrock is highly resistant to erosion.

Despite these limitations, our proposed process model provides an explanation for the presence of solid and dispersed basal ice facies at Mendenhall Glacier's terminus. While we did not find the lower interface of the frozen fringe layer, our field observations show that the greatest sediment concentrations were located near the base of the ice column. From theory, we know that the sediment concentration in the frozen fringe is inherited from the porosity of the underlying till matrix, leading to basal ice facies with elevated ($> 20\%$ concentrations) (Rempel, 2008). In the field, we observed a diffuse contact between the solid and dispersed facies, which can be explained by the loss of particles from the upper portion of the frozen fringe via thermal regelation, and our qualitative observations of individual particles suspended within an ice matrix are consistent with the process of thermal regelation. Thermal regelation requires a vertical temperature gradient, but given an isothermal ice mass, we only need to invoke the change in pressure-melting point with depth and the formation of a frozen fringe to provide enough of a gradient for the dispersed layer to form. Because vertical regelation only begins when the frozen fringe forms, and particles tend to have a migration rate that is not dependent on grain size (You et al., 2021), a clean contact occurs between the dispersed facies and the interior of the ice mass, also consistent with field observations.

Using our coupled models of ice flow and sediment entrainment, we find that the predicted thicknesses of dispersed basal ice layers at the terminus range between 0.2 and 1.8 m, depending largely on the sliding behavior of the glacier. In the field, we observed layers between 1.6 and 2 m, which would only be possible under our `SLOW` suite of model scenarios, with effective pressure scaled to 25% or greater of overburden pressure. From a process perspective, comparisons between our modeled and observed debris-rich ice layers help to constrain key environmental variables at the base of the glacier. The `SLOW` scenario configuration implies less rapid sliding at the base, with 25-35% of surface velocity explained by deformation; this is constrast to the `FAST` configuration, where sliding accounts for roughly 95% of observed surface motion. Further, elevated long-term mean effective pressure (low mean water pressure) would suggest that the hydrologic system is composed of relatively efficient channelized features (Arnold & Sharp, 1992; Flowers, 2015). This is consistent with previous work at Mendenhall Glacier that found meters-scale conduits near the end of the melt season (Gimbert et al., 2016). Future work should consider coupling the sediment entrainment model proposed here to a process model of subglacial hydrology to investigate how short-term (diurnal to seasonal) and small-scale variability in hydrology might influence sediment entrainment.

There are several existing hypotheses for the formation of dispersed basal ice facies, and it is unlikely that there is a sole mechanism responsible for entraining sediment within the ice column. Previous work has invoked pressure regelation of ice into the sediment matrix (Iverson, 1993; Knight, 1994), which is an attractive mechanism because it is plausible in any scenario where a temperate basal ice layer rests on till, thus helping to explain the prevalence of dispersed facies throughout a wide variety of glacial systems. However, models of frozen fringe formation rely on the same mechanism (pressure-induced infiltration), at the same interface (between the ice and till), and improve upon the physical parameterization of pressure-induced regelation (Rempel et al., 2004; Wettlaufer & Worster, 2006; Rempel, 2008; Meyer et al., 2019). Other work has proposed that basal adfreezing may form dispersed ice layers (Hart, 1995; Cuffey et al., 2000; Alley et al., 1997; Christoffersen et al., 2006), and while this may well be true beneath cold-based glaciers, it does not provide a sufficient explanation for the formation of dispersed ice beneath warm-bedded glaciers. Similarly, glacial-tectonic deformation could explain observations of folded, sheared, and otherwise deformed packages of dispersed basal ice

facies (Lawson, 1979; Sharp et al., 1994; Hubbard & Sharp, 1995; Alley et al., 1997; Cook, Swift, et al., 2011), especially where a steep icefall or overdeepening amplifies deformation within basal ice layers (Cook, Swift, et al., 2011). Alternatively, laboratory results have suggested that hydraulic supercooling may flush the interior of the ice matrix with fine sediment, creating a similarly *dispersed* (Hubbard et al., 2009; Cook, Graham, et al., 2011), *amber* (Cuffey et al., 2000), or *clotted* (Knight, 1994) facies. It is undoubtedly true that many of these prior hypotheses are active in specific settings; at Mendenhall Glacier, however, we observe dispersed basal ice facies without extensive signs of shear or deformation, without the presence of ogives or prominent icefalls (c.f. (Cook, Swift, et al., 2011)), and with many large particles (O[$10^{-1}$] m] that could not have been emplaced by fluvial transport. The process model we propose in this work provides a mechanism for the formation of dispersed basal ice facies that is very likely to be active in a wide variety of glacial settings, and does not exclude other processes that may co-occur beneath the same ice mass.

Building upon our understanding of these sediment entrainment processes allows us to present a first-order estimate of sediment fluxes transported by basal ice at Mendenhall Glacier. In general, sediment fluxes from both the frozen fringe and dispersed layer increase with the long-term, mean effective pressure. In model runs where the dispersed layer thickness falls within the uncertainty range of our field observations, the sediment flux from the frozen fringe ranged from 22,280 $m^3$ $a^{-1}$ to 38,640 $m^3$ $a^{-1}$. The total flux from the dispersed layer was 3 - 6% of that value, depending on the scenario, ranging from 976 $m^3$ $a^{-1}$ to 1,170 $m^3$ $a^{-1}$. At Svinafellsjökull, in Iceland, previous work estimated a sediment flux from the dispersed layer of 1.6 to $3.2\times10^3$ $m^3$ $a^{-1}$ (Cook, Swift, et al., 2011). However, the dispersed layer at the Svinafellsjökull terminus was nearly 3.5 m in thickness, for a glacier of comparable width and velocity. If we expect the sediment yield to scale with layer thickness between the two glaciers, Svinafellsjökull should export 45-50% more sediment than Mendenhall Glacier, which would place our model results within the lower range of values reported previously.

If all the sediment delivered to the terminus in basal ice layers each year is distributed over Mendenhall Lake (approximately 4.75 $km^2$ in 2021, digitized from Google Earth imagery), ignoring the processes of shoaling, moraine formation, and export at the far end of the lake, the deposition rate would range from 9.4 mm $a^{-1}$ to 1.62 cm $a^{-1}$ under our most realistic scenarios. Lake fill rates from Alaskan proglacial lakes are typically on the order of centimeters per year (Loso et al., 2004; Boes et al., 2017), or locally meters per year for surging glaciers (Fleisher et al., 2003). Given that Mendenhall Glacier covers an area of approximately 109 $km^2$, it would take an average specific erosion rate of less than 1 mm $a^{-1}$ to produce this volume of sediment, less than most typical erosion rates beneath alpine glaciers worldwide (Cook et al., 2020; Herman et al., 2021). However, when we consider that there are other mechanisms for glacial sediment transport, it is reasonable to assume that the contribution from basal ice composes a part, but not the entirety, of the overall sediment budget for a given proglacial lake.

Given the grounding zone configuration in 2021, Mendenhall distributes basal sediment between its terminal moraine and proglacial lake. However, our model also has important implications for sediment transport in marine-terminating glacier systems. In tidewater glacier systems, entrained sediment is transported by ice shelves and icebergs into the marine environment, where it is eventually deposited as ice-rafted debris (Bond et al., 1992; Broecker et al., 1992; Andrews & Tedesco, 1992). As ice mass travels, whether connected to the glacier as a shelf or floating freely as a berg, relatively warmer water in the fjord or coastal ocean drives melting and eventual rain-out of any entrained debris. In many systems, we observe deposits of ice-rafted debris beyond a tidewater glacier's grounding zone, which may be related to historical terminus positions (e.g., (Jennings et al., 2022)) or the spatial pattern of melt and rainout (e.g., (McGlannan et al., 2017)). Previous work has considered the role of basal sediment entrainment in governing the

flux of ice-rafted debris entering a fjord system (Alley & MacAyeal, 1994; Meyer et al., 2019), but basal ice stratigraphy may play an important role in increasing the distance at which debris may be transported before melting out. While the frozen fringe composes the majority of the entrained debris by mass, and melts earliest in transit beneath an ice shelf or iceberg, it insulates the dispersed layer from basal melt, allowing that material to be carried further into the coastal ocean (or, in alpine systems, into the proglacial lake). Thus, the dispersed basal ice layer may represent a significant source of sediment supply beyond the grounding zone of such a system.

Overall, our process models indicate that frozen fringe processes drive basal sediment entrainment beneath glaciers and ice sheets, but the specifics of basal ice stratigraphy are important for understanding the long-term behavior of the subglacial system, as well as the spatial patterns of sediment entrainment and deposition. Future work should focus on scaling laboratory experiments to the range of parameters relevant to subglacial environments, gathering archives of basal ice facies from a wider variety of glacial settings, and incorporating glacial sediment transport into more complex models of hydrology and ice dynamics.

## 8 Conclusions

At the margins of glaciers across a wide variety of climate and geologic settings, we observe a distinct sequence of solid and dispersed basal ice facies. We show how a process model of sediment entrainment through frozen fringe, followed by redistribution from thermal regelation, explains the co-evolution of these basal ice layers. We present a case study from Mendenhall Glacier, where we found continuous debris-rich ice layers across the land-terminating portion of the glacier's terminus. Using IGM's data assimilation module, we retrieve the glacier's modern-day stress balance and basal velocity field from observed surface ice velocities, glacier topography, and modeled ice thickness profiles. With this modeling framework, we estimate the total flux of sediment reaching Mendenhall Glacier's terminus within basal ice, and partition this flux between the two basal ice layers.

Co-occurring dispersed and solid basal ice facies have been documented in glaciers in Alaska (Lawson, 1979; Sharp et al., 1994), Iceland (Cook, Swift, et al., 2011), the European Alps (Hubbard & Sharp, 1995), Greenland (Knight, 1997), and Antarctica (Cuffey et al., 2000). A process model based on frozen fringe physics provides an attractive explanation for these features, as it relies on relatively few assumptions about the glacial, climatic, or geologic setting, and does not require us to fully resolve the three-dimensional enthalpy or stress fields within the glacier. Once a frozen fringe is in place, it provides all of the necessary physical conditions for particles to undergo regelation. While there are certainly other localized processes that induce or influence sediment entrainment beneath glaciers and ice sheets, frozen fringe evolution and thermal regelation provide a plausible explanation for the widespread occurrence of debris-rich ice layers in glaciers across many diverse regions. With this process knowledge, we can incorporate sediment transport by basal ice into landscape evolution models, better partition the sediment budgets of modern glaciers between subglacial fluvial and glacial processes, and improve our understanding of how glaciers entrain and distribute sediment across Earth's surface.

## Appendix A Full numerical model results

Section 4 describes the experimental design for the plan-view, 2.5D model runs; selected results are shown in Section 6. From IGM, we identified two plausible basal sliding scenarios, termed `FAST` and `SLOW`, corresponding to changes in main stem velocity. We then scaled the effective pressure from 5% to 40% of ice overburden pressure, as discussed in Section 4, in increments of 5%. Because the effective pressure scaling only changed the quantitative sediment flux results, but not the qualitative spatial patterns of sedi-

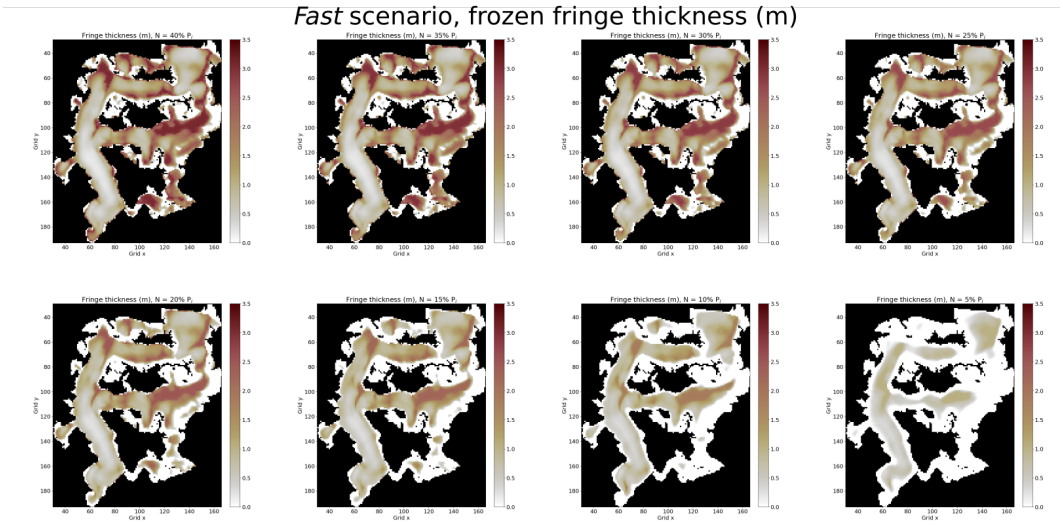


**Figure A1.** Final frozen fringe thickness from the `FAST` configuration model runs. Each plot shows results from a different effective pressure scaling.

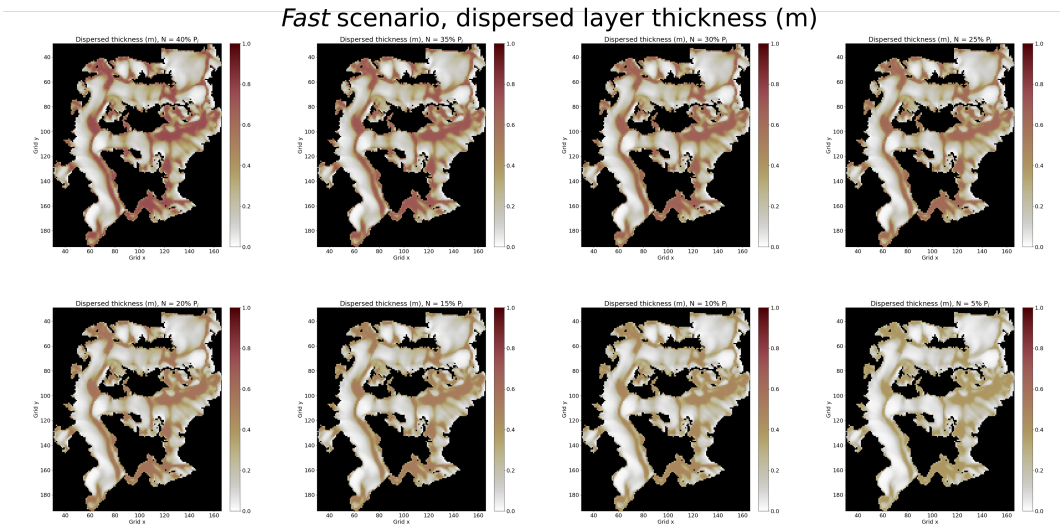


**Figure A2.** Final dispersed layer thickness from the `FAST` configuration model runs. Each plot shows results from a different effective pressure scaling.

ment entrainment, we only display the end-member scenarios in the main text. Here, we include all results from the suite of finalized model runs.

## Open Research

The field observations used to guide and validate model development are available at Pierce and Overeem (2024) [dataset submitted to PANGAEA, DOI pending] under a CC-BY: Creative Commons Attribution 4.0 International license. *Field data are included for peer review in the attached OpenDocument Spreadsheet file: "outcrop-data-mendenhall-glacier-2021.ods".* Interpolated, "best-fit" ice thickness and bedrock geometry fields were obtained from the Ice Thickness Model Intercomparison eXperiment (IT-

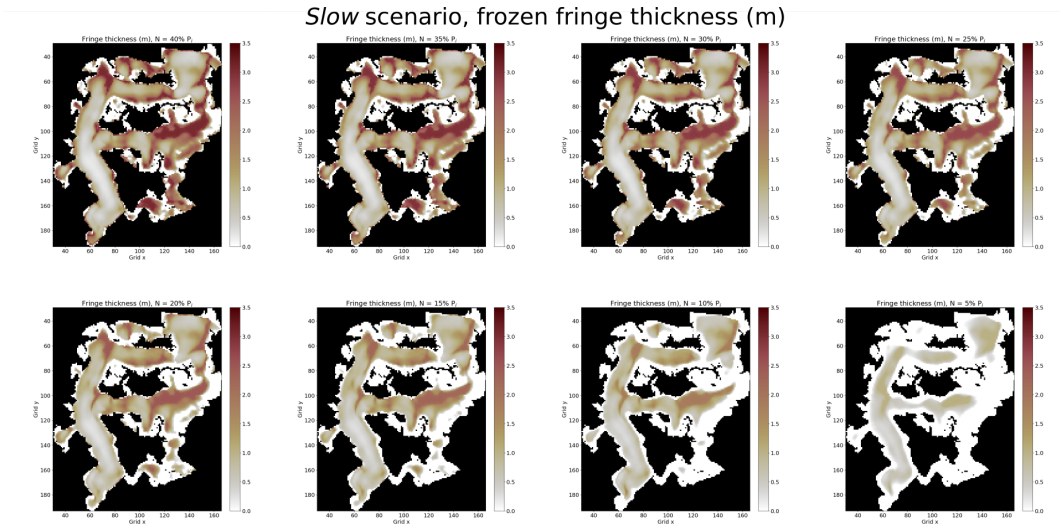


**Figure A3.** Final frozen fringe thickness from the `SLOW` configuration model runs. Each plot shows results from a different effective pressure scaling.

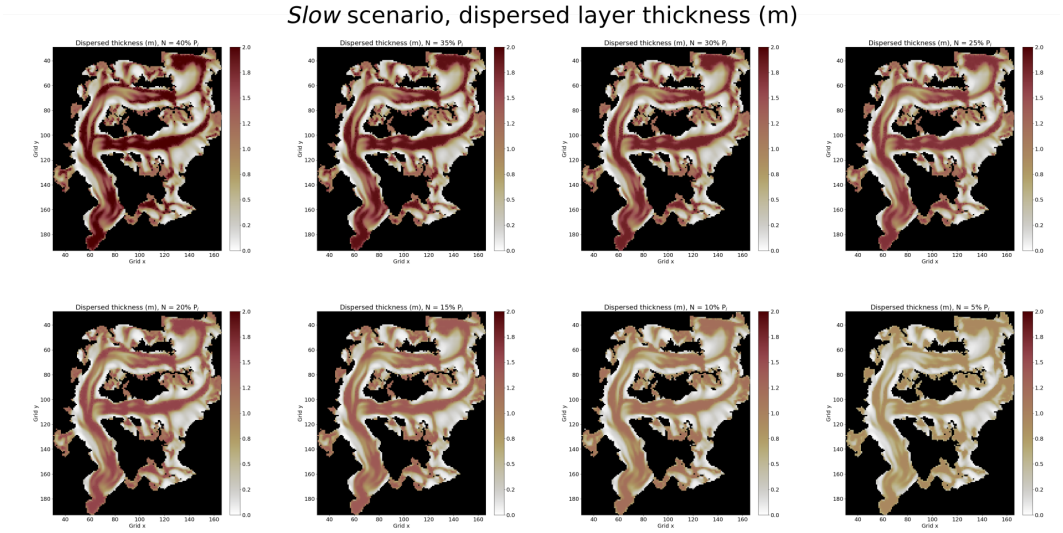


**Figure A4.** Final dispersed layer thickness from the `SLOW` configuration model runs. Each plot shows results from a different effective pressure scaling.

MIX) (Farinotti et al., 2019, 2021), available at http://dx.doi.org/10.5905/ethz-1007-92. Observed surface velocity data were obtained from the Inter-Mission Time Series of Land Ice Velocity and Elevation (ITS_LIVE) project from NASA's Making Earth System Data Records for Use in Research Environments (MEaSUREs) program (A. Gardner et al., 2022), accessed from the data portal at https://nsidc.org/apps/itslive/. The Instructed Glacier Model (IGM) is an open source model, described in (Jouvet, 2023; Jouvet & Cordonnier, 2023), and is available under the GNU General Public License v3.0 at https://github.com/jouvetg/igm. The numerical model described in this manuscript is also open source and available under the GNU General Public License v3.0 at https://github.com/ethan-pierce/mendenhall-glacier. *The software repository does not have a preliminary DOI, but this statement will be updated before publication to include a specific, tagged release and accompanying DOI for the software version used to generate finalized results.*

## References


Alley, R. B., Anandakrishnan, S., Dupont, T. K., Parizek, B. R., & Pollard, D. (2007, March). Effect of Sedimentation on Ice-Sheet Grounding-Line Stability. *Science*, *315*(5820), 1838–1841. Retrieved 2023-06-06, from https://www.science.org/doi/full/10.1126/science.1138396 (Publisher: American Association for the Advancement of Science) doi: 10.1126/science.1138396

Alley, R. B., Cuffey, K. M., Evenson, E. B., Strasser, J. C., Lawson, D. E., & Larson, G. J. (1997, January). How glaciers entrain and transport basal sediment: Physical constraints. *Quaternary Science Reviews*, *16*(9), 1017–1038. Retrieved 2019-11-30, from http://www.sciencedirect.com/science/article/pii/S0277379197000346 doi: 10.1016/S0277-3791(97)00034-6

Alley, R. B., Cuffey, K. M., & Zoet, L. K. (2019, December). Glacial erosion: status and outlook. *Annals of Glaciology*, *60*(80), 1–13. Retrieved 2022-12-23, from https://www.cambridge.org/core/journals/annals-of-glaciology/article/glacial-erosion-status-and-outlook/647A8088831114E528E9D506DBF0962A (Publisher: Cambridge University Press) doi: 10.1017/aog.2019.38

Alley, R. B., & MacAyeal, D. R. (1994). Ice-rafted debris associated with binge/purge oscillations of the Laurentide Ice Sheet. *Paleoceanography*, *9*(4), 503–511. Retrieved 2019-11-30, from https://agupubs.onlinelibrary.wiley.com/doi/abs/10.1029/94PA01008 doi: 10.1029/94PA01008

Andrews, J. T., & Tedesco, K. (1992, December). Detrital carbonate-rich sediments, northwestern Labrador Sea: Implications for ice-sheet dynamics and iceberg rafting (Heinrich) events in the North Atlantic. *Geology*, *20*(12), 1087–1090. Retrieved 2019-11-30, from https://pubs.geoscienceworld.org/geology/article-abstract/20/12/1087/187184/Detrital-carbonate-rich-sediments-northwestern doi: 10.1130/0091-7613(1992)020⟨1087:DCRSNL⟩2.3.CO;2

Arnold, N., & Sharp, M. (1992). Influence of glacier hydrology on the dynamics of a large Quaternary ice sheet. *Journal of Quaternary Science*, *7*(2), 109–124. Retrieved 2023-01-01, from https://onlinelibrary.wiley.com/doi/abs/10.1002/jqs.3390070204 (_eprint: https://onlinelibrary.wiley.com/doi/pdf/10.1002/jqs.3390070204) doi: 10.1002/jqs.3390070204

Arnold, N., & Sharp, M. (2002, February). Flow variability in the Scandinavian ice sheet: modelling the coupling between ice sheet flow and hydrology. *Quaternary Science Reviews*, *21*(4), 485–502. Retrieved 2023-01-01, from https://www.sciencedirect.com/science/article/pii/S0277379101000592 doi: 10.1016/S0277-3791(01)00059-2

Aschwanden, A., Bueler, E., Khroulev, C., & Blatter, H. (2012). An enthalpy formulation for glaciers and ice sheets. *Journal of Glaciology*, *58*(209), 441–457. Retrieved 2022-10-17, from https://www.cambridge.org/core/journals/journal-of-glaciology/article/an-enthalpy-formulation-for-glaciers-and-ice-sheets/605D2EC3DE03B82F2A8289220E76EB27 (Publisher: Cambridge University Press) doi: 10.3189/2012JoG11J088

Barnhart, K. R., Hutton, E. W. H., Tucker, G. E., Gasparini, N. M., Istanbulluoglu, E., Hobley, D. E. J., ... Bandaragoda, C. (2020, May). Short communication: Landlab v2.0: a software package for Earth surface dynamics. *Earth Surface Dynamics*, *8*(2), 379–397. Retrieved 2023-04-03, from https://esurf.copernicus.org/articles/8/379/2020/ (Publisher: Copernicus GmbH) doi: 10.5194/esurf-8-379-2020

Batchelor, C. L., & Dowdeswell, J. A. (2015, May). Ice-sheet grounding-zone wedges (GZWs) on high-latitude continental margins. *Marine Geology*, *363*, 65–92. Retrieved 2023-06-06, from https://www.sciencedirect.com/science/article/pii/S0025322715000304 doi: 10.1016/j.margeo.2015.02.001

Baydin, A. G., Pearlmutter, B. A., Radul, A. A., & Siskind, J. M. (2018). Automatic Differentiation in Machine Learning: a Survey. *Journal of Machine Learning Research*, *18*(153), 1–43. Retrieved 2023-06-07, from http://jmlr.org/papers/v18/17-468.html

Blatter, H., & Hutter, K. (1991). Polythermal conditions in arctic glaciers. *Journal of Glaciology*, *37*(126), 261–269. Retrieved 2022-10-17, from https://www.cambridge.org/core/journals/journal-of-glaciology/article/polythermal-conditions-in-arctic-glaciers/FB1252B8C43257103B2505853E30693D (Publisher: Cambridge University Press) doi: 10.3189/S0022143000007279

Boes, E., Van Daele, M., Moernaut, J., Schmidt, S., Jensen, B. J., Praet, N., ... De Batist, M. (2017, November). Varve formation during the past three centuries in three large proglacial lakes in south-central Alaska. *GSA Bulletin*, *130*(5-6), 757–774. Retrieved 2023-04-05, from https://doi.org/10.1130/B31792.1 doi: 10.1130/B31792.1

Bond, G., Heinrich, H., Broecker, W., Labeyrie, L., McManus, J., Andrews, J., ... Ivy, S. (1992, November). Evidence for massive discharges of icebergs into the North Atlantic ocean during the last glacial period. *Nature*, *360*(6401), 245–249. Retrieved 2019-11-30, from https://www.nature.com/articles/360245a0 doi: 10.1038/360245a0

Broecker, W., Bond, G., Klas, M., Clark, E., & McManus, J. (1992, January). Origin of the northern Atlantic's Heinrich events. *Climate Dynamics*, *6*(3), 265–273. Retrieved 2022-10-28, from https://doi.org/10.1007/BF00193540 doi: 10.1007/BF00193540

Christoffersen, P., Tulaczyk, S., Carsey, F. D., & Behar, A. E. (2006). A quantitative framework for interpretation of basal ice facies formed by ice accretion over subglacial sediment. *Journal of Geophysical Research: Earth Surface*, *111*(F1). Retrieved 2023-01-04, from https://onlinelibrary.wiley.com/doi/abs/10.1029/2005JF000363 (_eprint: https://onlinelibrary.wiley.com/doi/pdf/10.1029/2005JF000363) doi: 10.1029/2005JF000363

Cook, S. J., Graham, D. J., Swift, D. A., Midgley, N. G., & Adam, W. G. (2011, January). Sedimentary signatures of basal ice formation and their preservation in ice-marginal sediments. *Geomorphology*, *125*(1), 122–131. Retrieved 2019-11-30, from http://www.sciencedirect.com/science/article/pii/S0169555X10004009 doi: 10.1016/j.geomorph.2010.08.018

Cook, S. J., Swift, D. A., Graham, D. J., & Midgley, N. G. (2011). Origin and significance of 'dispersed facies' basal ice: Svínafellsjökull, Iceland. *Journal of Glaciology*, *57*(204), 710–720. Retrieved 2022-10-28, from

https://www.cambridge.org/core/journals/journal-of-glaciology/article/origin-and-significance-of-dispersed-facies-basal-ice-svinafellsjokull-iceland/6C0833A71E59A9161FB8B6D24217B396 (Publisher: Cambridge University Press) doi: 10.3189/002214311797409703

Cook, S. J., Swift, D. A., Kirkbride, M. P., Knight, P. G., & Waller, R. I. (2020, February). The empirical basis for modelling glacial erosion rates. *Nature Communications*, *11*(1), 759. Retrieved 2022-10-17, from https://www.nature.com/articles/s41467-020-14583-8 (Number: 1 Publisher: Nature Publishing Group) doi: 10.1038/s41467-020-14583-8

Cuffey, K. M., Conway, H., Gades, A. M., Hallet, B., Lorrain, R., Severinghaus, J. P., ... White, J. W. C. (2000, April). Entrainment at cold glacier beds. *Geology*, *28*(4), 351–354. Retrieved 2023-01-04, from https://doi.org/10.1130/0091-7613(2000)28<351:EACGB>2.0.CO;2 doi: 10.1130/0091-7613(2000)28⟨351:EACGB⟩2.0.CO;2

Cuffey, K. M., & Paterson, W. S. B. (2010). *The Physics of Glaciers*. Academic Press. (Google-Books-ID: Jca2v1u1EKEC)

Delaney, I., & Adhikari, S. (2020). Increased Subglacial Sediment Discharge in a Warming Climate: Consideration of Ice Dynamics, Glacial Erosion, and Fluvial Sediment Transport. *Geophysical Research Letters*, *47*(7), e2019GL085672. Retrieved 2022-10-28, from https://onlinelibrary.wiley.com/doi/abs/10.1029/2019GL085672 (_eprint: https://onlinelibrary.wiley.com/doi/pdf/10.1029/2019GL085672) doi: 10.1029/2019GL085672

Delaney, I., Werder, M. A., & Farinotti, D. (2019). A Numerical Model for Fluvial Transport of Subglacial Sediment. *Journal of Geophysical Research: Earth Surface*, *124*(8), 2197–2223. Retrieved 2023-04-05, from https://onlinelibrary.wiley.com/doi/abs/10.1029/2019JF005004 (_eprint: https://onlinelibrary.wiley.com/doi/pdf/10.1029/2019JF005004) doi: 10.1029/2019JF005004

Delmas, M., Calvet, M., & Gunnell, Y. (2009, March). Variability of Quaternary glacial erosion rates – A global perspective with special reference to the Eastern Pyrenees. *Quaternary Science Reviews*, *28*(5), 484–498. Retrieved 2022-12-23, from https://www.sciencedirect.com/science/article/pii/S0277379108003375 doi: 10.1016/j.quascirev.2008.11.006

Evans, D. J. A., & Benn, D. I. (2014). *A Practical Guide to the Study of Glacial Sediments*. Routledge. (Google-Books-ID: 11hpAwAAQBAJ)

Farinotti, D., Brinkerhoff, D. J., Fürst, J. J., Gantayat, P., Gillet-Chaulet, F., Huss, M., ... Andreassen, L. M. (2021). Results from the Ice Thickness Models Intercomparison eXperiment Phase 2 (ITMIX2). *Frontiers in Earth Science*, *8*. Retrieved 2022-12-23, from https://www.frontiersin.org/articles/10.3389/feart.2020.571923

Farinotti, D., Huss, M., Fürst, J. J., Landmann, J., Machguth, H., Maussion, F., & Pandit, A. (2019, March). A consensus estimate for the ice thickness distribution of all glaciers on Earth. *Nature Geoscience*, *12*(3), 168–173. Retrieved 2023-04-04, from https://www.nature.com/articles/s41561-019-0300-3 (Number: 3 Publisher: Nature Publishing Group) doi: 10.1038/s41561-019-0300-3

Fleisher, P. J., Bailey, P. K., & Cadwell, D. H. (2003, August). A decade of sedimentation in ice-contact, proglacial lakes, Bering Glacier, AK. *Sedimentary Geology*, *160*(4), 309–324. Retrieved 2023-04-05, from https://www.sciencedirect.com/science/article/pii/S0037073803000897 doi: 10.1016/S0037-0738(03)00089-7

Flowers, G. E. (2015, April). Modelling water flow under glaciers and ice sheets. *Proceedings of the Royal Society A: Mathematical, Physical and Engineering Sciences*, *471*(2176), 20140907. doi: 10.1098/rspa.2014.0907

Gardner, A., Fahnestock, M., & Scambos, T. (2022). *MEASURES ITS_live Regional Glacier and Ice Sheet Surface Velocities, Version 1.* NASA National Snow and Ice Data Center DAAC. Retrieved 2023-04-03, from https://nsidc.org/data/nsidc-0776/versions/1 doi: 10.5067/6II6VW8LLWJ7

Gardner, A. S., Moholdt, G., Scambos, T., Fahnstock, M., Ligtenberg, S., van den Broeke, M., & Nilsson, J. (2018, February). Increased West Antarctic and unchanged East Antarctic ice discharge over the last 7 years. *The Cryosphere*, *12*(2), 521–547. Retrieved 2023-11-02, from https://tc.copernicus.org/articles/12/521/2018/ (Publisher: Copernicus GmbH) doi: 10.5194/tc-12-521-2018

Gilbert, A., Gimbert, F., Thøgersen, K., Schuler, T. V., & Kääb, A. (2022). A Consistent Framework for Coupling Basal Friction With Subglacial Hydrology on Hard-Bedded Glaciers. *Geophysical Research Letters*, *49*(13), e2021GL097507. Retrieved 2023-11-01, from https://onlinelibrary.wiley.com/doi/abs/10.1029/2021GL097507 (_eprint: https://onlinelibrary.wiley.com/doi/pdf/10.1029/2021GL097507) doi: 10.1029/2021GL097507

Gilpin, R. R. (1979, February). A model of the "liquid-like" layer between ice and a substrate with applications to wire regelation and particle migration. *Journal of Colloid and Interface Science*, *68*(2), 235–251. Retrieved 2022-10-17, from https://www.sciencedirect.com/science/article/pii/0021979779902777 doi: 10.1016/0021-9797(79)90277-7

Gimbert, F., Tsai, V. C., Amundson, J. M., Bartholomaus, T. C., & Walter, J. I. (2016). Subseasonal changes observed in subglacial channel pressure, size, and sediment transport. *Geophysical Research Letters*, *43*(8), 3786–3794. Retrieved 2022-12-19, from https://onlinelibrary.wiley.com/doi/abs/10.1002/2016GL068337 (_eprint: https://onlinelibrary.wiley.com/doi/pdf/10.1002/2016GL068337) doi: 10.1002/2016GL068337

Hansen, D. D., & Zoet, L. K. (2022). Characterizing Sediment Flux of Deforming Glacier Beds. *Journal of Geophysical Research: Earth Surface*, *127*(4), e2021JF006544. Retrieved 2023-04-05, from https://onlinelibrary.wiley.com/doi/abs/10.1029/2021JF006544 (_eprint: https://onlinelibrary.wiley.com/doi/pdf/10.1029/2021JF006544) doi: 10.1029/2021JF006544

Hart, J. K. (1995). An investigation of the deforming layer/debris-rich basal-ice continuum, illustrated from three Alaskan glaciers. *Journal of Glaciology*, *41*(139), 619–633. Retrieved 2023-01-04, from https://www.cambridge.org/core/journals/journal-of-glaciology/article/an-investigation-of-the-deforming-layerdebrisrich-basalice-continuum-illustrated-from-three-alaskan-glaciers/8098CD1A7CB13BDB6A4800BAF4FD4C8B (Publisher: Cambridge University Press) doi: 10.3189/S0022143000034936

Herman, F., De Doncker, F., Delaney, I., Prasicek, G., & Koppes, M. (2021, June). The impact of glaciers on mountain erosion. *Nature Reviews Earth & Environment*, *2*(6), 422–435. Retrieved 2022-10-17, from https://www.nature.com/articles/s43017-021-00165-9 (Number: 6 Publisher: Nature Publishing Group) doi: 10.1038/s43017-021-00165-9

Hewitt, I. J., & Schoof, C. (2017, February). Models for polythermal ice sheets and glaciers. *The Cryosphere*, *11*(1), 541–551. Retrieved 2022-06-18, from https://tc.copernicus.org/articles/11/541/2017/ doi: 10.5194/tc-11-541-2017

Hildes, D. H. D., Clarke, G. K. C., Flowers, G. E., & Marshall, S. J. (2004, February). Subglacial erosion and englacial sediment transport modelled for North American ice sheets. *Quaternary Science Reviews*, *23*(3), 409–430. Retrieved 2019-11-30, from http://www.sciencedirect.com/science/article/pii/

S0277379103002877 doi: 10.1016/j.quascirev.2003.06.005

Hodson, A. J., & Ferguson, R. I. (1999). Fluvial suspended sediment transport from cold and warm-based glaciers in Svalbard. *Earth Surface Processes and Landforms*, *24*(11), 957–974. Retrieved 2022-10-04, from https://onlinelibrary.wiley.com/doi/abs/10.1002/%28SICI%291096-9837%28199910%2924%3A11%3C957%3A%3AAID-ESP19%3E3.0.CO%3B2-J (_eprint: https://onlinelibrary.wiley.com/doi/pdf/10.1002/%28SICI%291096-9837%28199910%2924%3A11%3C957%3A%3AAID-ESP19%3E3.0.CO%3B2-J) doi: 10.1002/(SICI)1096-9837(199910)24:11⟨957::AID-ESP19⟩3.0.CO;2-J

Hoffman, A. O., Christianson, K., Holschuh, N., Case, E., Kingslake, J., & Arthern, R. (2022). The Impact of Basal Roughness on Inland Thwaites Glacier Sliding. *Geophysical Research Letters*, *49*(14), e2021GL096564. Retrieved 2023-11-01, from https://onlinelibrary.wiley.com/doi/abs/10.1029/2021GL096564 (_eprint: https://onlinelibrary.wiley.com/doi/pdf/10.1029/2021GL096564) doi: 10.1029/2021GL096564

Hubbard, B., Cook, S., & Coulson, H. (2009, September). Basal ice facies: a review and unifying approach. *Quaternary Science Reviews*, *28*(19), 1956–1969. Retrieved 2022-10-28, from https://www.sciencedirect.com/science/article/pii/S0277379109000882 doi: 10.1016/j.quascirev.2009.03.005

Hubbard, B., & Sharp, M. (1995, November). Basal Ice Fades and Their Formation in the Western Alps. *Arctic and Alpine Research*, *27*(4), 301–310. Retrieved 2023-01-04, from https://www.tandfonline.com/doi/abs/10.1080/00040851.1995.12003127 (Publisher: Taylor & Francis _eprint: https://www.tandfonline.com/doi/pdf/10.1080/00040851.1995.12003127) doi: 10.1080/00040851.1995.12003127

Iverson, N. R. (1993, June). Regelation of ice through debris at glacier beds: Implications for sediment transport. *Geology*, *21*(6), 559–562. Retrieved 2019-11-30, from https://pubs.geoscienceworld.org/geology/article-abstract/21/6/559/205928/Regelation-of-ice-through-debris-at-glacier-beds doi: 10.1130/0091-7613(1993)021⟨0559:ROITDA⟩2.3.CO;2

Iverson, N. R., Baker, R. W., Hooke, R. L., Hanson, B., & Jansson, P. (1999). Coupling between a glacier and a soft bed: I. A relation between effective pressure and local shear stress determined from till elasticity. *Journal of Glaciology*, *45*(149), 31–40. Retrieved 2023-04-05, from https://www.cambridge.org/core/journals/journal-of-glaciology/article/coupling-between-a-glacier-and-a-soft-bed-i-a-relation-between-effective-pressure-and-local-shear-stress-determined-from-till-elasticity/626A836AB49B09977F500D1112A3CC72 (Publisher: Cambridge University Press) doi: 10.3189/S0022143000003014

Iverson, N. R., & Semmens, D. J. (1995). Intrusion of ice into porous media by regelation: A mechanism of sediment entrainment by glaciers. *Journal of Geophysical Research: Solid Earth*, *100*(B6), 10219–10230. Retrieved 2019-12-10, from http://agupubs.onlinelibrary.wiley.com/doi/abs/10.1029/95JB00043 doi: 10.1029/95JB00043

Jennings, A., Reilly, B., Andrews, J., Hogan, K., Walczak, M., Jakobsson, M., ... Troelstra, S. R. (2022, May). Modern and early Holocene ice shelf sediment facies from Petermann Fjord and northern Nares Strait, northwest Greenland. *Quaternary Science Reviews*, *283*, 107460. Retrieved 2023-01-04, from https://www.sciencedirect.com/science/article/pii/S0277379122000919 doi: 10.1016/j.quascirev.2022.107460

Jouvet, G. (2023, February). Inversion of a Stokes glacier flow model emulated by deep learning. *Journal of Glaciology*, *69*(273), 13–26. Retrieved 2023-04-04, from https://www.cambridge.org/core/journals/journal-of-glaciology/article/inversion-of-a-stokes-glacier-flow-model-emulated-by-deep-learning/40A3BBE3E1747E1D93B37C57268748DF

(Publisher: Cambridge University Press) doi: 10.1017/jog.2022.41

Jouvet, G., & Cordonnier, G. (2023, September). Ice-flow model emulator based on physics-informed deep learning. *Journal of Glaciology*, 1–15. Retrieved 2023-11-01, from https://www.cambridge.org/core/journals/journal-of-glaciology/article/iceflow-model-emulator-based-on-physicsinformed-deep-learning/8C4D103C0F34DA690D9B524DF1461C5C (Publisher: Cambridge University Press) doi: 10.1017/jog.2023.73

Jouvet, G., Cordonnier, G., Kim, B., Lüthi, M., Vieli, A., & Aschwanden, A. (2022, August). Deep learning speeds up ice flow modelling by several orders of magnitude. *Journal of Glaciology*, *68*(270), 651–664. Retrieved 2023-04-04, from https://www.cambridge.org/core/journals/journal-of-glaciology/article/deep-learning-speeds-up-ice-flow-modelling-by-several-orders-of-magnitude/748E962A103D2AF45F4CA8823C88C0C0 (Publisher: Cambridge University Press) doi: 10.1017/jog.2021.120

Kharazmi, E., Zhang, Z., & Karniadakis, G. E. (2019, November). *Variational Physics-Informed Neural Networks For Solving Partial Differential Equations.* arXiv. Retrieved 2023-11-01, from http://arxiv.org/abs/1912.00873 (arXiv:1912.00873 [physics, stat]) doi: 10.48550/arXiv.1912.00873

Knight, P. G. (1994, November). Two-facies interpretation of the basal layer of the Greenland ice sheet contributes to a unified model of basal ice formation. *Geology*, *22*(11), 971–974. Retrieved 2022-12-23, from https://doi.org/10.1130/0091-7613(1994)022<0971:TFIOTB>2.3.CO;2 doi: 10.1130/0091-7613(1994)022⟨0971:TFIOTB⟩2.3.CO;2

Knight, P. G. (1997, January). The basal ice layer of glaciers and ice sheets. *Quaternary Science Reviews*, *16*(9), 975–993. Retrieved 2022-10-28, from https://www.sciencedirect.com/science/article/pii/S0277379197000334 doi: 10.1016/S0277-3791(97)00033-4

Knight, P. G., Waller, R. I., Patterson, C. J., Jones, A. P., & Robinson, Z. P. (2002). Discharge of debris from ice at the margin of the Greenland ice sheet. *Journal of Glaciology*, *48*(161), 192–198. Retrieved 2022-12-23, from https://www.cambridge.org/core/journals/journal-of-glaciology/article/discharge-of-debris-from-ice-at-the-margin-of-the-greenland-ice-sheet/9CA9352556B059BD2350103FD768A735 (Publisher: Cambridge University Press) doi: 10.3189/172756502781831359

Köpfli, M., Gräff, D., Lipovsky, B. P., Selvadurai, P. A., Farinotti, D., & Walter, F. (2022). Hydraulic Conditions for Stick-Slip Tremor Beneath an Alpine Glacier. *Geophysical Research Letters*, *49*(21), e2022GL100286. Retrieved 2023-11-01, from https://onlinelibrary.wiley.com/doi/abs/10.1029/2022GL100286 (_eprint: https://onlinelibrary.wiley.com/doi/pdf/10.1029/2022GL100286) doi: 10.1029/2022GL100286

Lawson, D. E. (1979, May). *Sedimentological analysis of the western terminus region of the Matanuska Glacier, Alaska* (Report). Cold Regions Research and Engineering Laboratory (U.S.). Retrieved 2022-12-23, from https://erdc-library.erdc.dren.mil/jspui/handle/11681/9016 (Accepted: 2016-06-20T13:39:52Z Publication Title: This Digital Resource was created from scans of the Print Resource)

Loso, M. G., Anderson, R. S., & Anderson, S. P. (2004, December). Post–Little Ice Age record of coarse and fine clastic sedimentation in an Alaskan proglacial lake. *Geology*, *32*(12), 1065–1068. Retrieved 2023-04-05, from https://doi.org/10.1130/G20839.1 doi: 10.1130/G20839.1

McGlannan, A. J., Bart, P. J., Chow, J. M., & DeCesare, M. (2017, October). On the influence of post-LGM ice shelf loss and grounding zone sedimentation on West Antarctic ice sheet stability. *Marine Geology*, *392*, 151–169. Retrieved 2023-01-04, from https://www.sciencedirect.com/science/article/pii/S002532271730097X doi: 10.1016/j.margeo.2017.08.005

Meyer, C. R., Robel, A. A., & Rempel, A. W. (2019, October). Frozen fringe explains sediment freeze-on during Heinrich events. *Earth and Planetary Science Letters*, *524*, 115725. Retrieved 2022-10-10, from https://www.sciencedirect.com/science/article/pii/S0012821X19304170 doi: 10.1016/j.epsl.2019.115725

Meyer, C. R., Schoof, C., & Rempel, A. W. (2021, September). *A thermomechanical model for frost heave and subglacial frozen fringe.* arXiv. Retrieved 2022-10-17, from http://arxiv.org/abs/2109.12182 (arXiv:2109.12182 [physics]) doi: 10.48550/arXiv.2109.12182

Motyka, R. J., O'Neel, S., Connor, C. L., & Echelmeyer, K. A. (2003, January). Twentieth century thinning of Mendenhall Glacier, Alaska, and its relationship to climate, lake calving, and glacier run-off. *Global and Planetary Change*, *35*(1), 93–112. Retrieved 2022-12-23, from https://www.sciencedirect.com/science/article/pii/S0921818102001388 doi: 10.1016/S0921-8181(02)00138-8

Nye, J. F. (1967, December). Theory of regelation. *The Philosophical Magazine: A Journal of Theoretical Experimental and Applied Physics*, *16*(144), 1249–1266. Retrieved 2022-10-17, from https://doi.org/10.1080/14786436708229974 (Publisher: Taylor & Francis _eprint: https://doi.org/10.1080/14786436708229974) doi: 10.1080/14786436708229974

Overeem, I., Hudson, B. D., Syvitski, J. P. M., Mikkelsen, A. B., Hasholt, B., Broeke, M. R. v. d., ... Morlighem, M. (2017, November). Substantial export of suspended sediment to the global oceans from glacial erosion in Greenland. *Nature Geoscience*, *10*(11), 859–863. Retrieved 2019-11-30, from https://www.nature.com/articles/ngeo3046 doi: 10.1038/ngeo3046

Pfeffer, W. T., Arendt, A. A., Bliss, A., Bolch, T., Cogley, J. G., Gardner, A. S., ... Consortium, T. R. (2014). The Randolph Glacier Inventory: a globally complete inventory of glaciers. *Journal of Glaciology*, *60*(221), 537–552. Retrieved 2022-12-23, from https://www.cambridge.org/core/journals/journal-of-glaciology/article/randolph-glacier-inventory-a-globally-complete-inventory-of-glaciers/730D4CC76E0E3EC1832FA3F4D90691CE (Publisher: Cambridge University Press) doi: 10.3189/2014JoG13J176

Porter, C., Morin, P., Howat, I., Noh, M.-J., Bates, B., Peterman, K., ... Bojesen, M. (2022, September). *ArcticDEM, Version 3.* Harvard Dataverse. Retrieved 2022-12-23, from https://dataverse.harvard.edu/dataset.xhtml?persistentId=doi:10.7910/DVN/OHHUKH doi: 10.7910/DVN/OHHUKH

Post, A., & LaChapelle, E. R. (2000). *Glacier Ice.* University of Toronto Press. (Google-Books-ID: BofiWpPh328C)

Powell, J. E., Tankersley, M., Ainsworth, T., Amundson, J. M., Armstrong, B., Botelho, B., ... Wilcox, P. (2022, July). *Juneau's Changing Climate and Community Response* (Report). Alaska Coastal Rainforest Center. Retrieved 2022-12-19, from https://scholarworks.alaska.edu/handle/11122/12930 (Accepted: 2022-07-19T19:50:19Z Journal Abbreviation: This work was supported by The Department of the Interior Alaska Climate Adaptation Science Center, which is managed by the USGS National Climate Adaptation Science Center.)

Raissi, M., Perdikaris, P., & Karniadakis, G. E. (2019, February). Physics-informed neural networks: A deep learning framework for solving forward and inverse problems involving nonlinear partial differential equations. *Journal of Computational Physics*, *378*, 686–707. Retrieved 2023-11-01, from https://www.sciencedirect.com/science/article/pii/S0021999118307125 doi: 10.1016/j.jcp.2018.10.045

Rempel, A. W. (2008). A theory for ice-till interactions and sediment entrainment beneath glaciers. *Journal of Geophysical Research:*

*Earth Surface*, *113*(F1). Retrieved 2022-10-10, from https://onlinelibrary.wiley.com/doi/abs/10.1029/2007JF000870 (_eprint: https://onlinelibrary.wiley.com/doi/pdf/10.1029/2007JF000870) doi: 10.1029/2007JF000870

Rempel, A. W., Wettlaufer, J. S., & Worster, M. G. (2004, January). Premelting dynamics in a continuum model of frost heave. *Journal of Fluid Mechanics*, *498*, 227–244. Retrieved 2022-10-10, from https://www.cambridge.org/core/journals/journal-of-fluid-mechanics/article/abs/premelting-dynamics-in-a-continuum-model-of-frost-heave/FD9B68C29CAE904A0F91CEF36E8DC0DD (Publisher: Cambridge University Press) doi: 10.1017/S0022112003006761

Riihimaki, C. A., MacGregor, K. R., Anderson, R. S., Anderson, S. P., & Loso, M. G. (2005). Sediment evacuation and glacial erosion rates at a small alpine glacier. *Journal of Geophysical Research: Earth Surface*, *110*(F3). Retrieved 2022-12-23, from https://onlinelibrary.wiley.com/doi/abs/10.1029/2004JF000189 (_eprint: https://onlinelibrary.wiley.com/doi/pdf/10.1029/2004JF000189) doi: 10.1029/2004JF000189

Rowan, A. V., Egholm, D. L., & Clark, C. D. (2022). Forward modelling of the completeness and preservation of palaeoclimate signals recorded by ice-marginal moraines. *Earth Surface Processes and Landforms*, *47*(9), 2198–2208. Retrieved 2023-06-06, from https://onlinelibrary.wiley.com/doi/abs/10.1002/esp.5371 (_eprint: https://onlinelibrary.wiley.com/doi/pdf/10.1002/esp.5371) doi: 10.1002/esp.5371

Schoof, C. (2010, January). Coulomb friction and other sliding laws in a higher-order glacier flow model. *Mathematical Models and Methods in Applied Sciences*, *20*(01), 157–189. Retrieved 2023-04-05, from https://www.worldscientific.com/doi/abs/10.1142/S0218202510004180 (Publisher: World Scientific Publishing Co.) doi: 10.1142/S0218202510004180

Sharp, M., Jouzel, J., Hubbard, B., & Lawson, W. (1994). The character, structure and origin of the basal ice layer of a surge-type glacier. *Journal of Glaciology*, *40*(135), 327–340. Retrieved 2023-01-04, from https://www.cambridge.org/core/journals/journal-of-glaciology/article/character-structure-and-origin-of-the-basal-ice-layer-of-a-surgetype-glacier/E580D08912FF5C3DC0D5CD8BD6DC4366 (Publisher: Cambridge University Press) doi: 10.3189/S0022143000007413

Sommers, A., Rajaram, H., & Morlighem, M. (2018, July). SHAKTI: Subglacial Hydrology and Kinetic, Transient Interactions v1.0. *Geoscientific Model Development*, *11*(7), 2955–2974. Retrieved 2023-04-05, from https://gmd.copernicus.org/articles/11/2955/2018/ (Publisher: Copernicus GmbH) doi: 10.5194/gmd-11-2955-2018

Swift, D. A., Nienow, P. W., & Hoey, T. B. (2005). Basal sediment evacuation by subglacial meltwater: suspended sediment transport from Haut Glacier d'Arolla, Switzerland. *Earth Surface Processes and Landforms*, *30*(7), 867–883. Retrieved 2022-10-04, from https://onlinelibrary.wiley.com/doi/abs/10.1002/esp.1197 (_eprint: https://onlinelibrary.wiley.com/doi/pdf/10.1002/esp.1197) doi: 10.1002/esp.1197

Syvitski, J. P. M., Andrews, J. T., & Dowdeswell, J. A. (1996, March). Sediment deposition in an iceberg-dominated glacimarine environment, East Greenland: basin fill implications. *Global and Planetary Change*, *12*(1), 251–270. Retrieved 2022-12-23, from https://www.sciencedirect.com/science/article/pii/0921818195000232 doi: 10.1016/0921-8181(95)00023-2

Team, P. (2017). *Planet Application Program Interface: In Space for Life on Earth.*

Planet. Retrieved from "https://api.planet.com"

Werder, M. A., Hewitt, I. J., Schoof, C. G., & Flowers, G. E. (2013). Modeling channelized and distributed subglacial drainage in two dimensions. *Journal of Geophysical Research: Earth Surface*, *118*(4), 2140–2158. Retrieved 2023-04-05, from https://onlinelibrary.wiley.com/doi/abs/10.1002/jgrf.20146 (_eprint: https://onlinelibrary.wiley.com/doi/pdf/10.1002/jgrf.20146) doi: 10.1002/jgrf.20146

Wettlaufer, J., & Worster, M. G. (2006, January). PREMELTING DYNAMICS. *Annual Review of Fluid Mechanics*, *38*(1), 427–452. Retrieved 2022-10-17, from https://www.annualreviews.org/doi/10.1146/annurev.fluid.37.061903.175758 doi: 10.1146/annurev.fluid.37.061903.175758

Wilson, F. H., Hults, C., Mull, C. G., & Karl, S. M. (2015). *Geologic map of Alaska* (Tech. Rep. No. 3340). U.S. Geological Survey. Retrieved 2024-01-11, from https://pubs.usgs.gov/publication/sim3340 (ISSN: 2329-132X Publication Title: Scientific Investigations Map) doi: 10.3133/sim3340

Woodard, J. B., Zoet, L. K., Iverson, N. R., & Helanow, C. (2023, April). Inferring forms of glacier slip laws from estimates of ice-bed separation during glacier slip. *Journal of Glaciology*, *69*(274), 324–332. Retrieved 2023-11-01, from https://www.cambridge.org/core/journals/journal-of-glaciology/article/inferring-forms-of-glacier-slip-laws-from-estimates-of-icebed-separation-during-glacier-slip/DA176C0C20579EF91EE1FA82611383C0 (Publisher: Cambridge University Press) doi: 10.1017/jog.2022.63

You, J., Wang, Z., & Grae Worster, M. (2021). Thermal regelation of single particles and particle clusters in ice. *Soft Matter*, *17*(7), 1779–1787. Retrieved 2022-10-17, from https://pubs.rsc.org/en/content/articlelanding/2021/sm/d0sm01547d (Publisher: Royal Society of Chemistry) doi: 10.1039/D0SM01547D

Zoet, L. K., & Iverson, N. R. (2020, April). A slip law for glaciers on deformable beds. *Science*, *368*(6486), 76–78. Retrieved 2023-01-01, from https://www.science.org/doi/full/10.1126/science.aaz1183 (Publisher: American Association for the Advancement of Science) doi: 10.1126/science.aaz1183

Zoet, L. K., Iverson, N. R., Andrews, L., & Helanow, C. (2021, December). Transient evolution of basal drag during glacier slip. *Journal of Glaciology*, 1–10. Retrieved 2022-06-16, from https://www.cambridge.org/core/journals/journal-of-glaciology/article/transient-evolution-of-basal-drag-during-glacier-slip/F76449FDA944213E4006BABAAD36758F (Publisher: Cambridge University Press) doi: 10.1017/jog.2021.131

**Figure 1.**

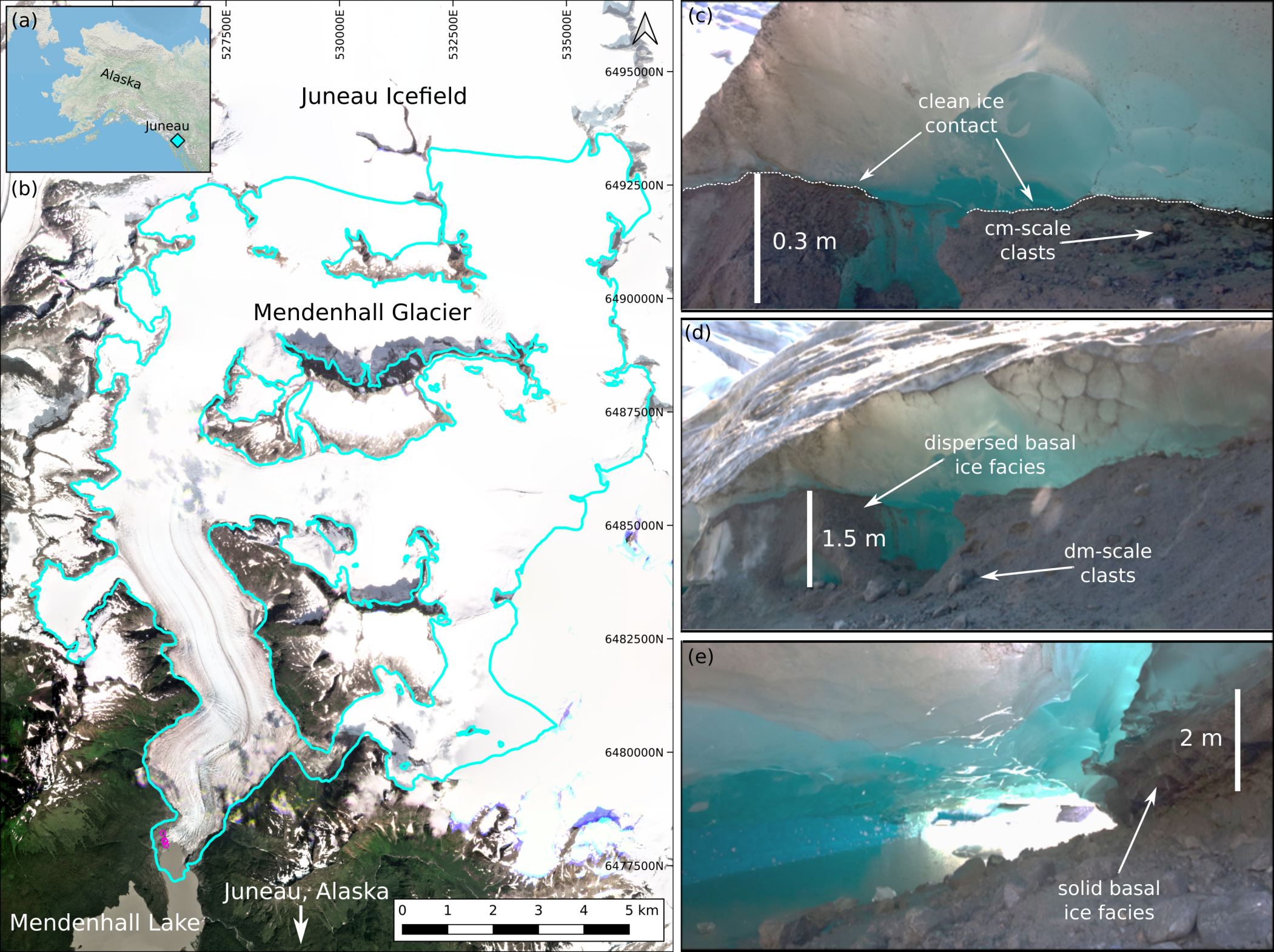
(a)
Alaska
Juneau
(b)
527500E
530000E
532500E
535000E
6495000N
6492500N
6490000N
6487500N
6485000N
6482500N
6480000N
6477500N
Juneau Icefield
Mendenhall Glacier
Juneau, Alaska
Mendenhall Lake
0 1 2 3 4 5 km
(c)
clean ice contact
0.3 m
cm-scale clasts
(d)
dispersed basal ice facies
1.5 m
dm-scale clasts
(e)
2 m
solid basal ice facies

**Figure 2.**

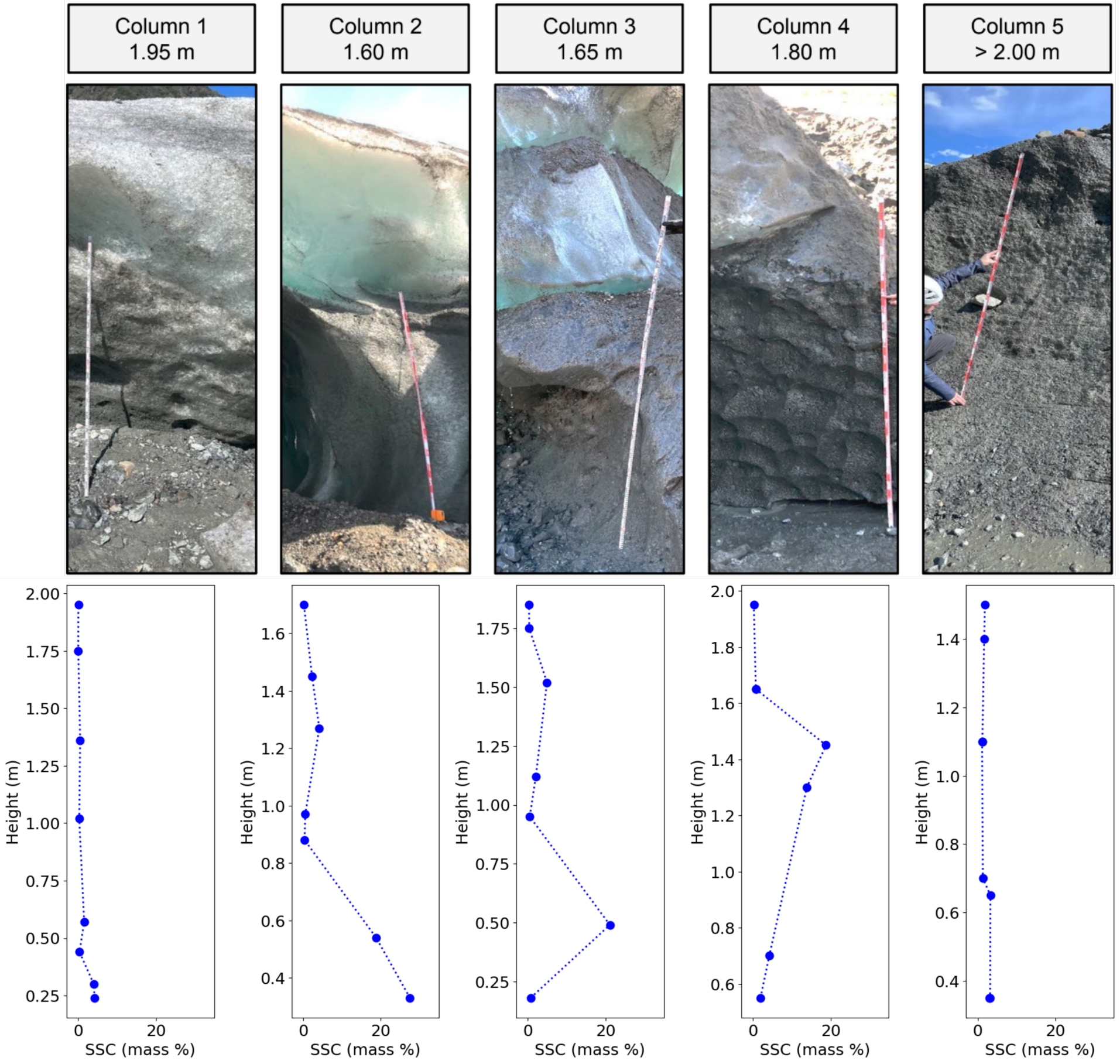
Column 1
1.95 m
Column 2
1.60 m
Column 3
1.65 m
Column 4
1.80 m
Column 5
> 2.00 m
Height (m)
SSC (mass %)

**Figure 3.**

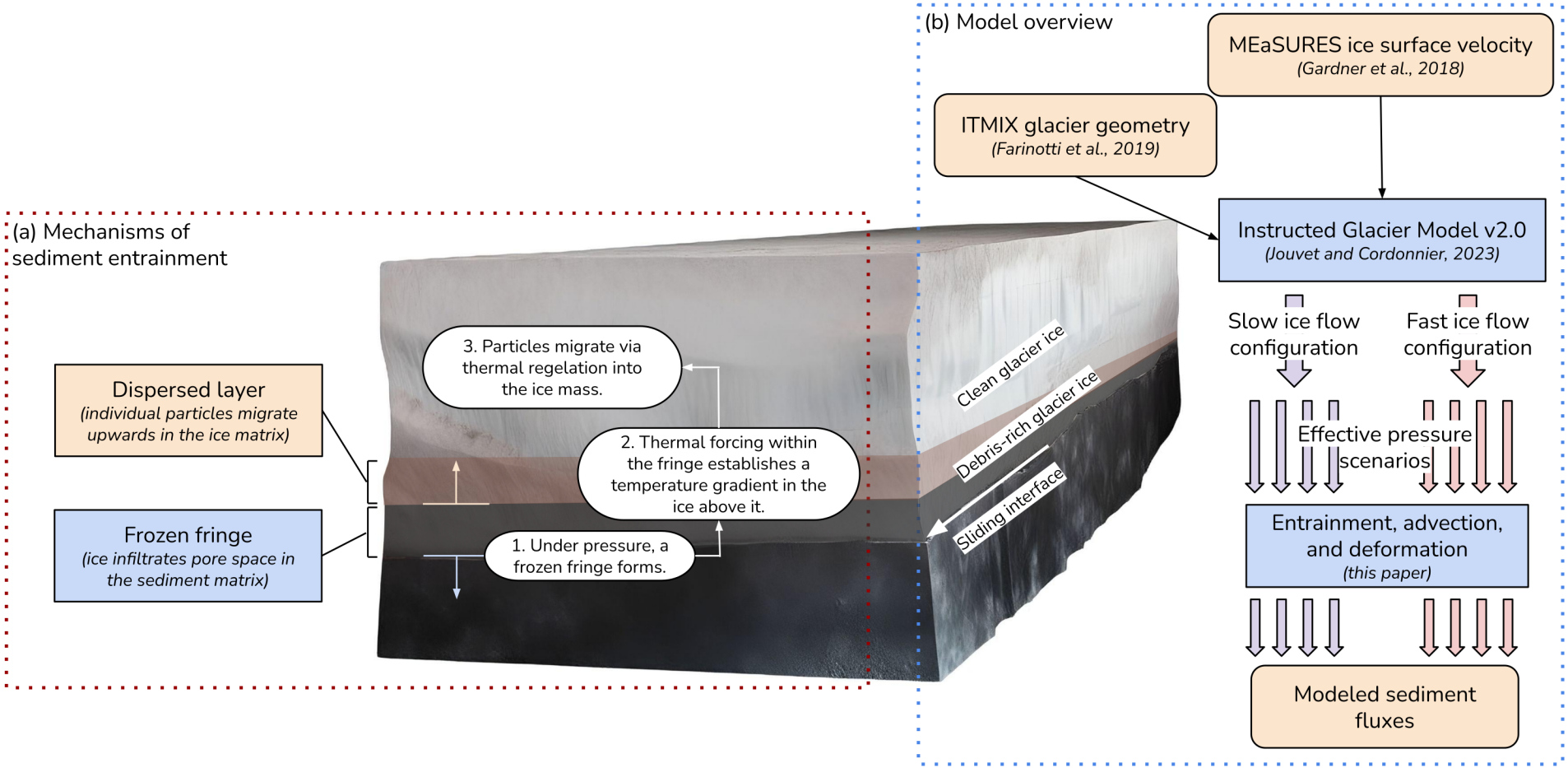
(a) Mechanisms of sediment entrainment
Dispersed layer
(individual particles migrate upwards in the ice matrix)
Frozen fringe
(ice infiltrates pore space in the sediment matrix)
3. Particles migrate via thermal regelation into the ice mass.
2. Thermal forcing within the fringe establishes a temperature gradient in the ice above it.
1. Under pressure, a frozen fringe forms.
Clean glacier ice
Debris-rich glacier ice
Sliding interface
(b) Model overview
MEaSURES ice surface velocity
(Gardner et al., 2018)
ITMIX glacier geometry
(Farinotti et al., 2019)
Instructed Glacier Model v2.0
(Jouvet and Cordonnier, 2023)
Slow ice flow configuration
Fast ice flow configuration
Effective pressure scenarios
Entrainment, advection, and deformation
(this paper)
Modeled sediment fluxes

**Figure 4.**

# Sensitivity experiments

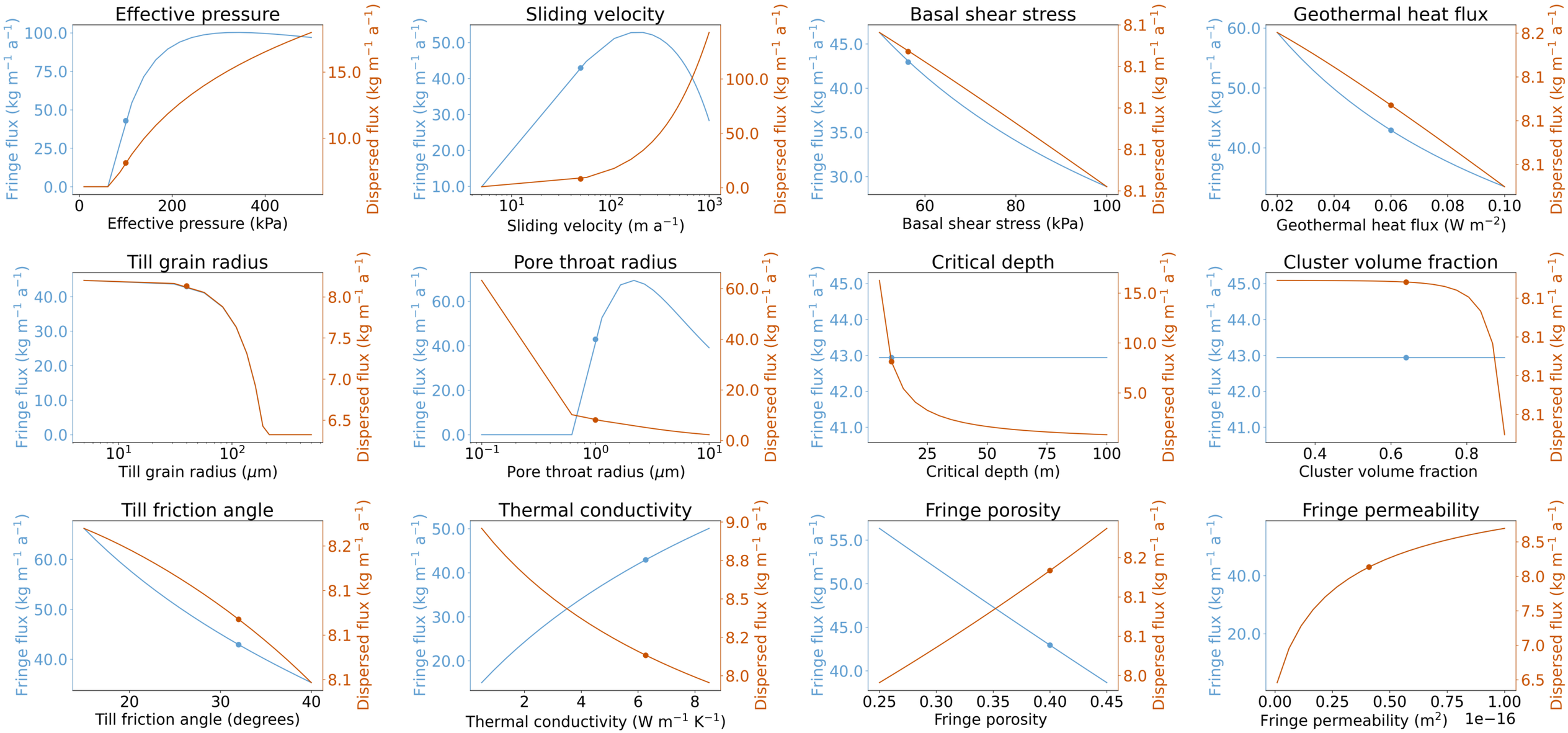


# Sensitivity Magnitude

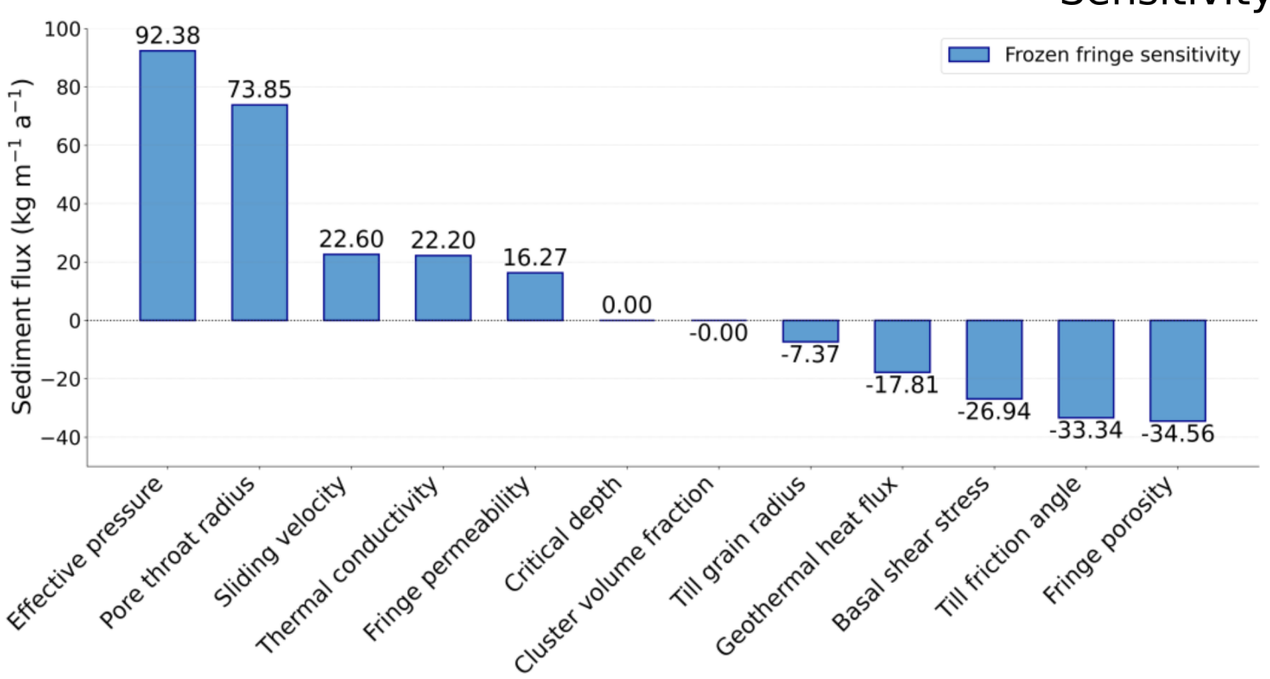


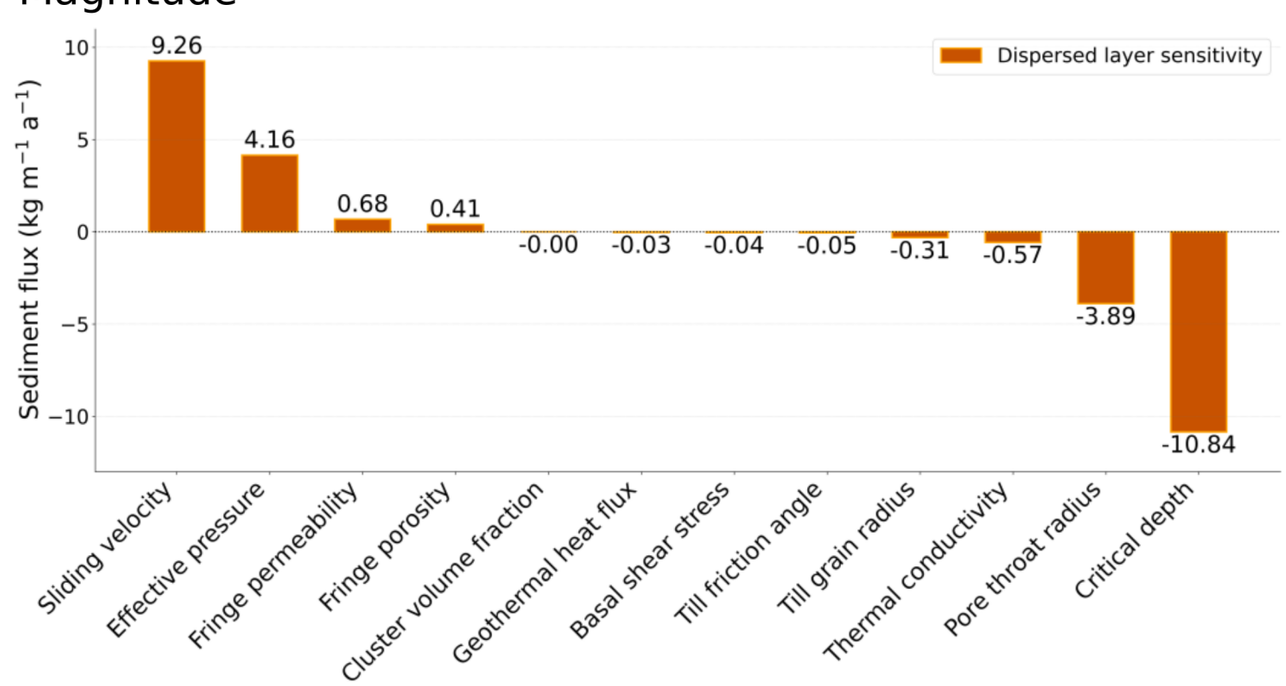

**Figure 5.**

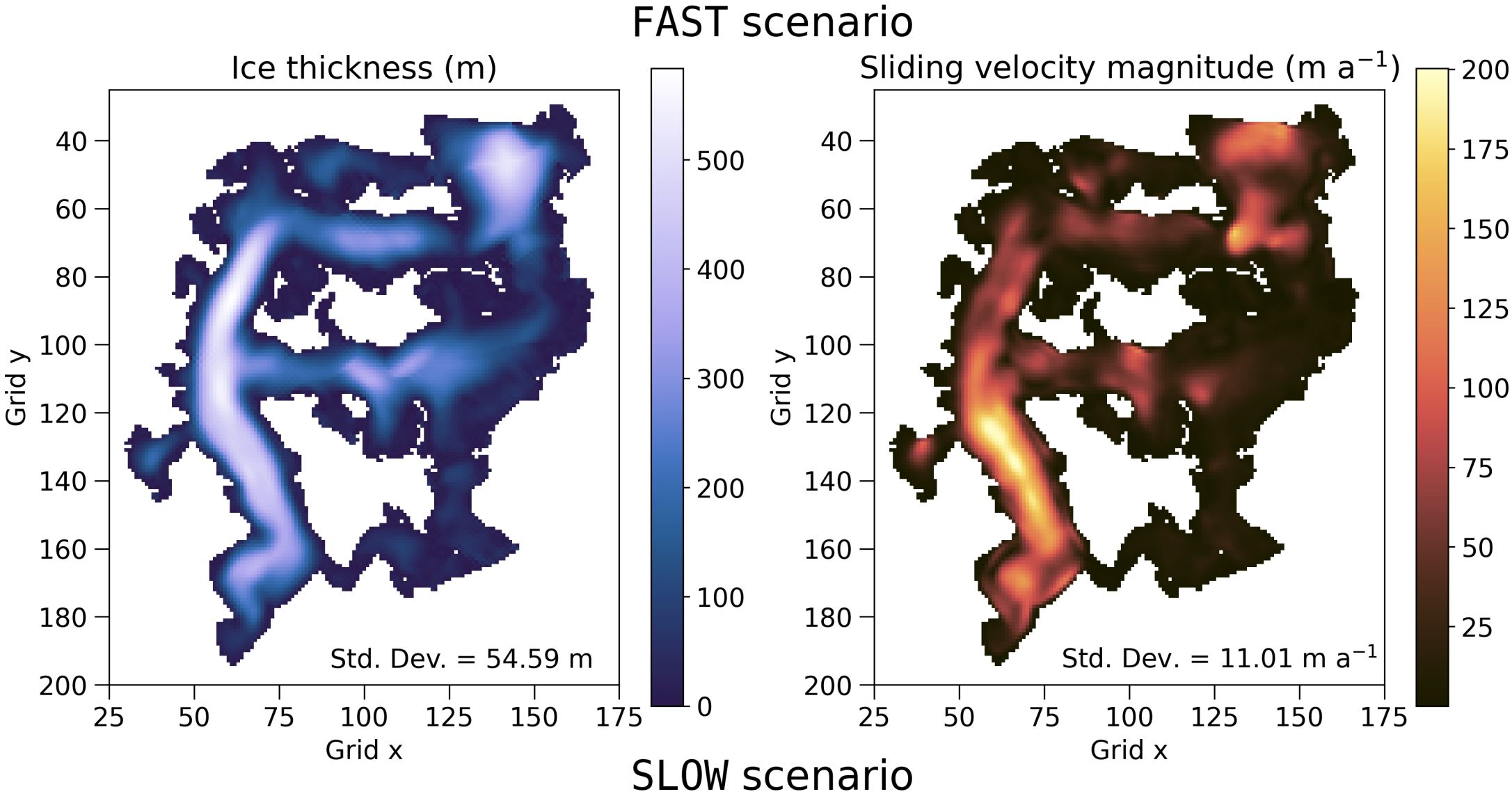
FAST scenario
Ice thickness (m)
Std. Dev. = 54.59 m
Sliding velocity magnitude (m a$^{-1}$)
Std. Dev. = 11.01 m a$^{-1}$
Grid y
Grid x
SLOW scenario
Ice thickness (m)
Std. Dev. = 62.06 m
Sliding velocity magnitude (m a$^{-1}$)
Std. Dev. = 9.99 m a$^{-1}$
Grid y
Grid x

**Figure 6.**

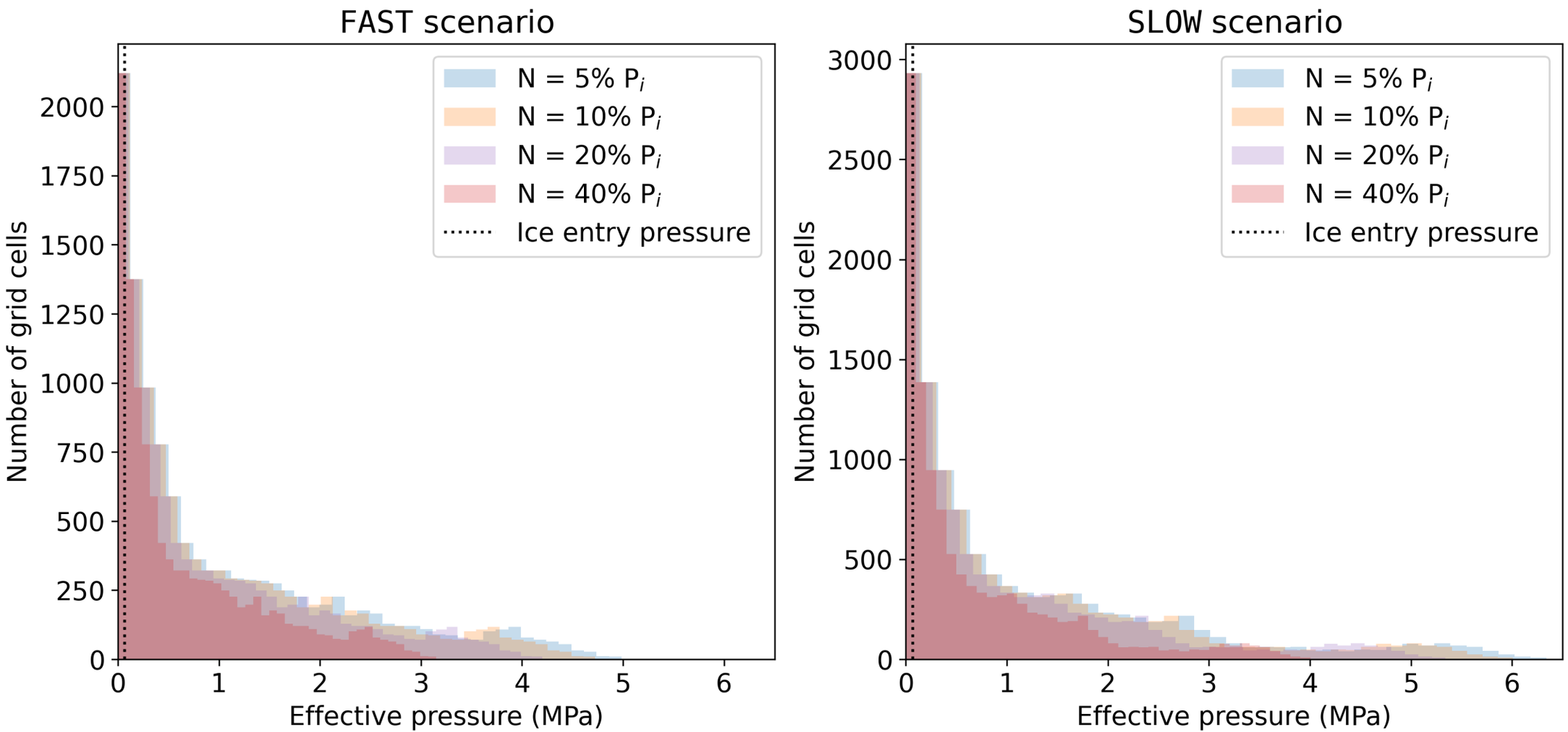
FAST scenario
SLOW scenario
N = 5% $P_i$
N = 10% $P_i$
N = 20% $P_i$
N = 40% $P_i$
Ice entry pressure
Number of grid cells
Effective pressure (MPa)
0
250
500
750
1000
1250
1500
1750
2000
2500
3000
1
2
3
4
5
6

**Figure 7.**

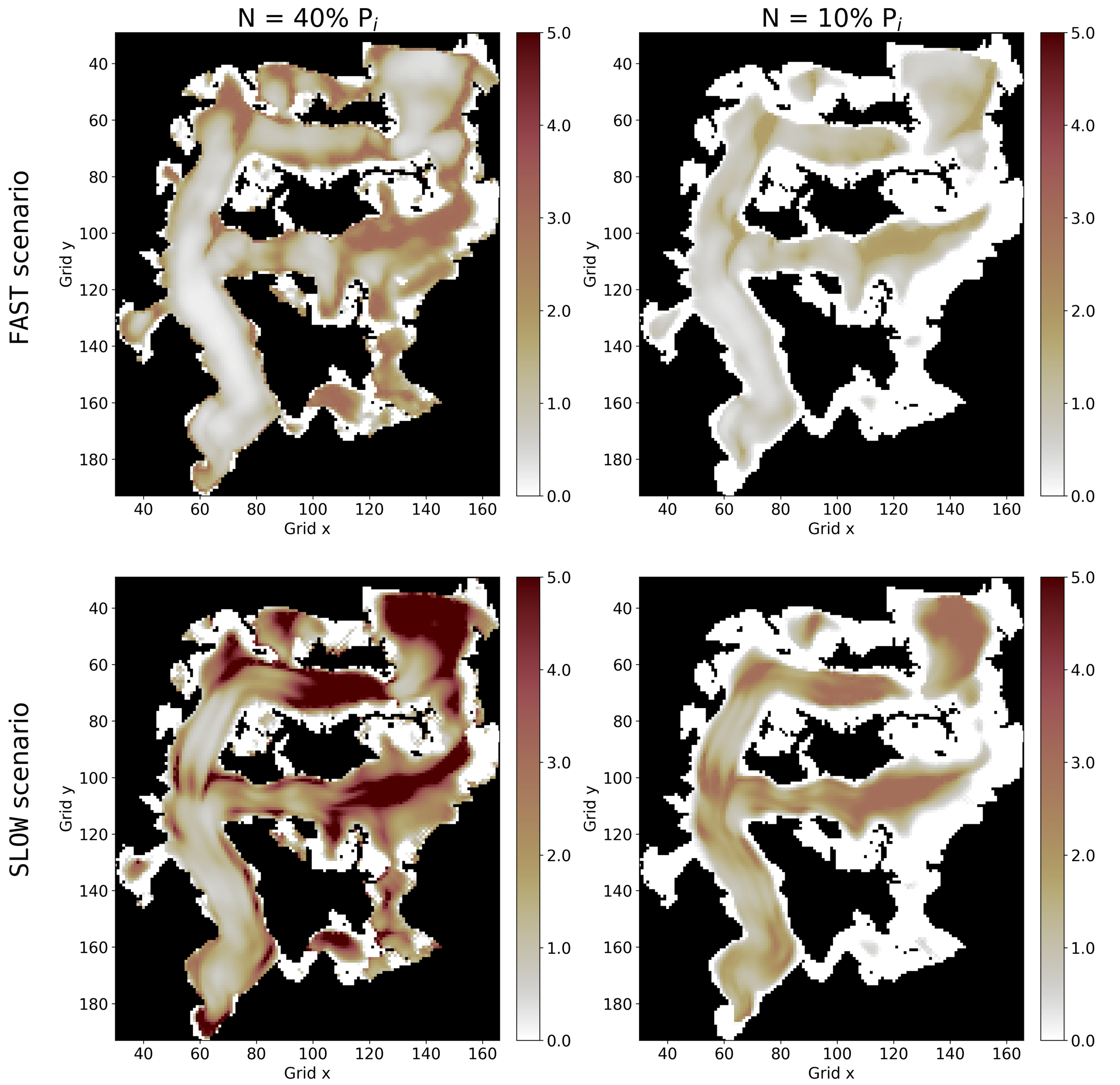
N = 40% $P_i$
N = 10% $P_i$
FAST scenario
SLOW scenario
Grid y
Grid x
40
60
80
100
120
140
160
180
0.0
1.0
2.0
3.0
4.0
5.0

**Figure 8.**

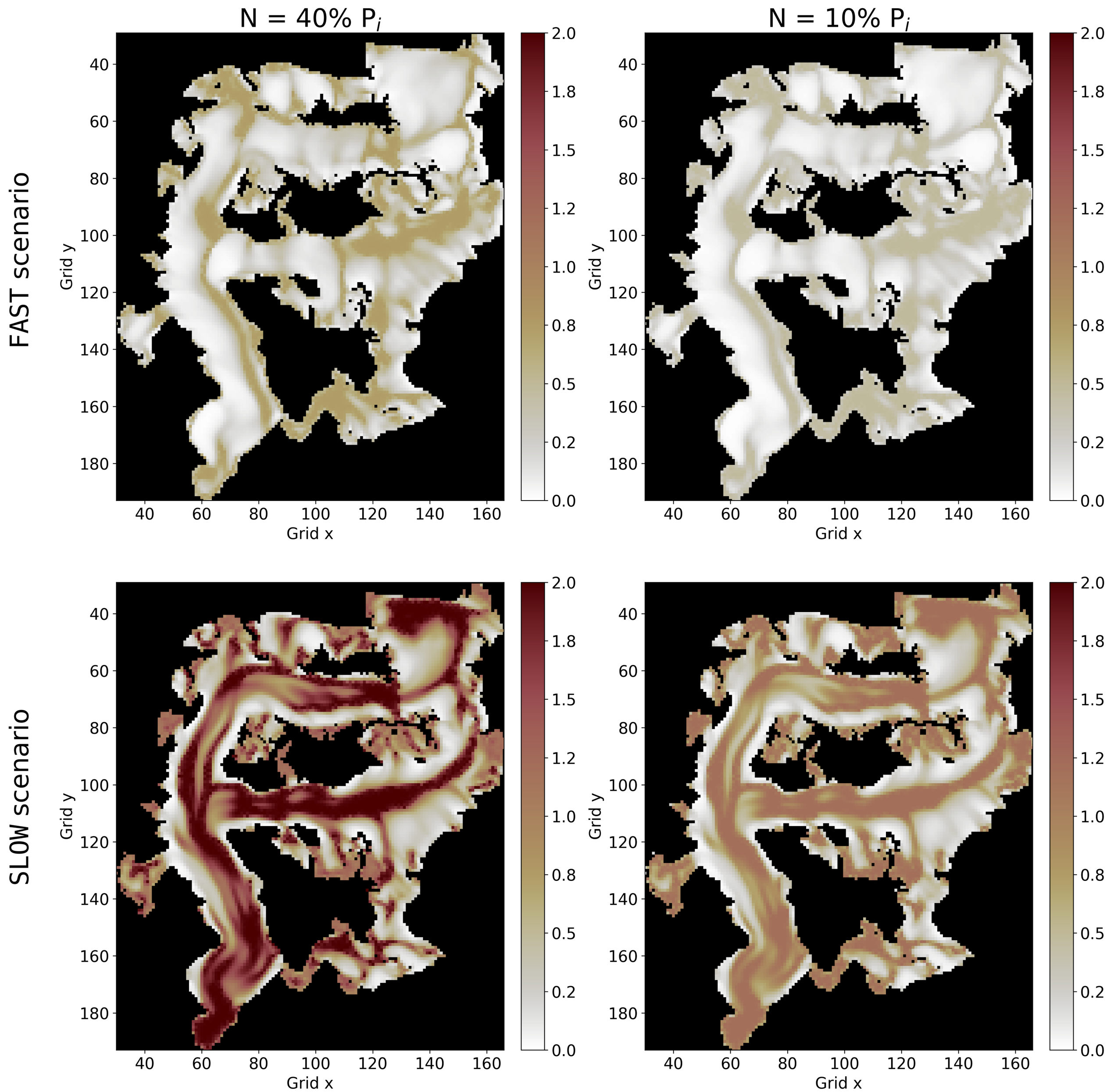
N = 40% $P_i$
N = 10% $P_i$
FAST scenario
SLOW scenario
Grid y
Grid x
40
60
80
100
120
140
160
180
0.0
0.2
0.5
0.8
1.0
1.2
1.5
1.8
2.0

**Figure 9.**

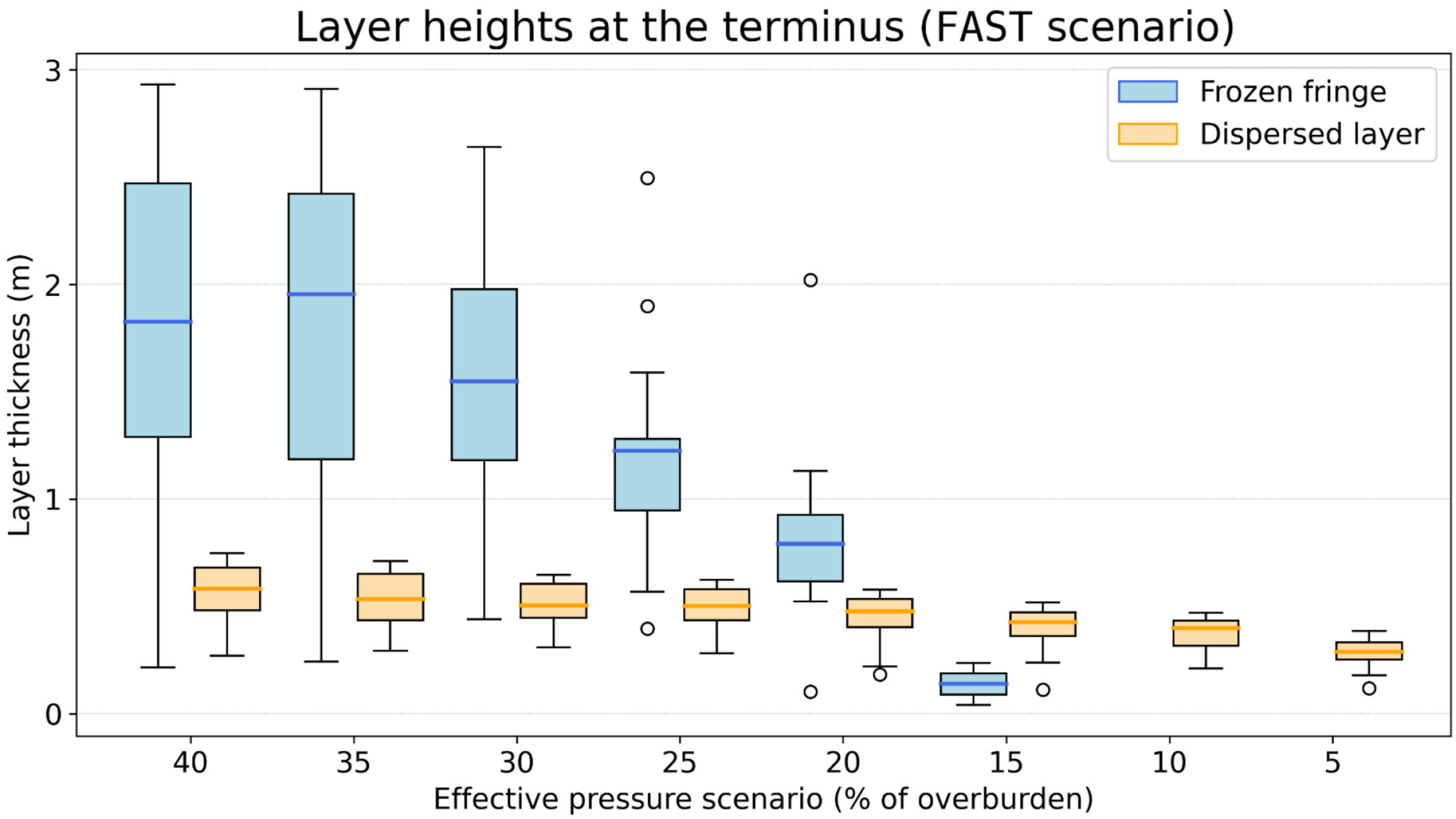
Layer heights at the terminus (FAST scenario)
Frozen fringe
Dispersed layer
Layer thickness (m)
0
1
2
3
40
35
30
25
20
15
10
5
Effective pressure scenario (% of overburden)

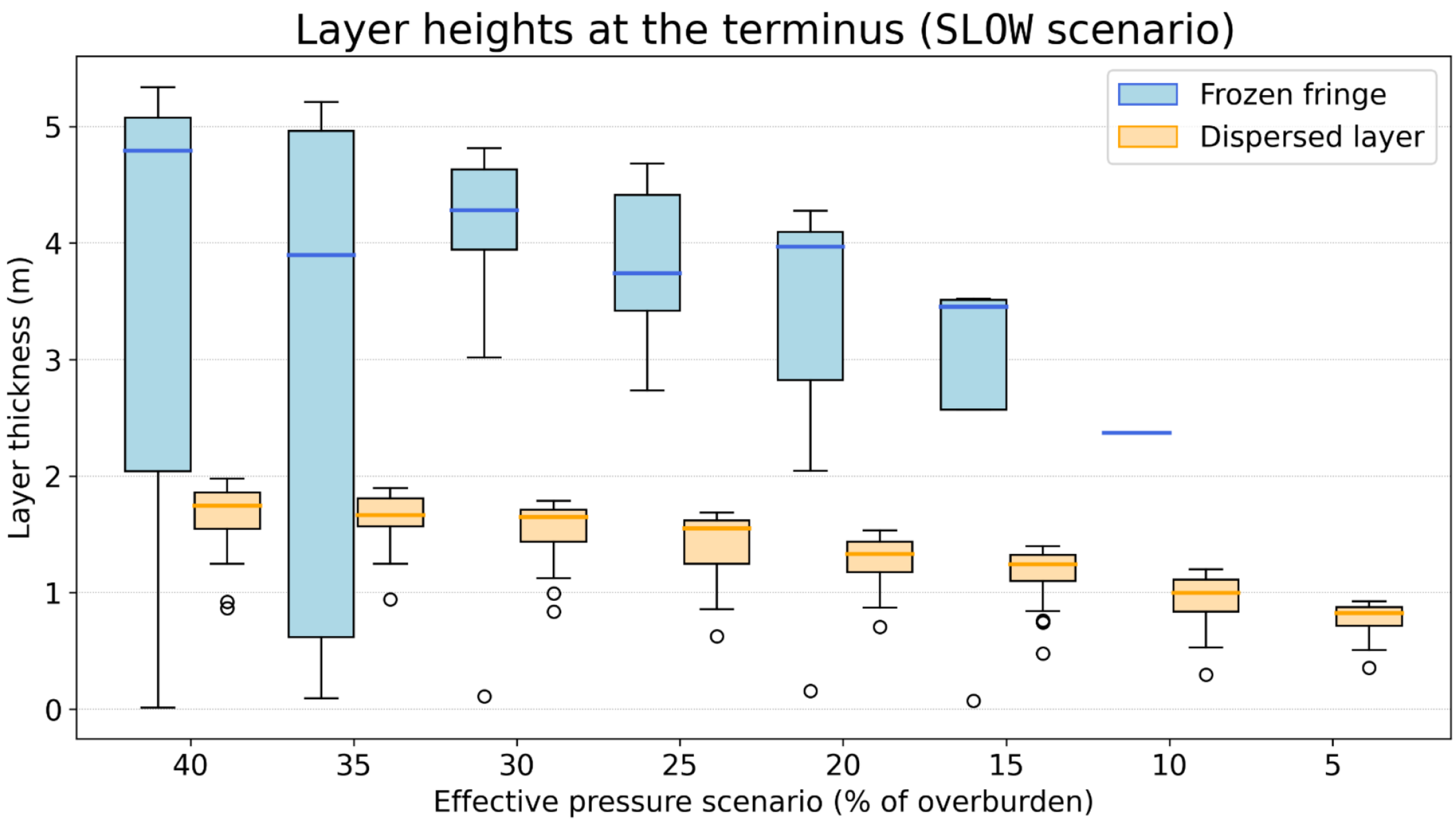
Layer heights at the terminus (SLOW scenario)
Frozen fringe
Dispersed layer
Layer thickness (m)
0
1
2
3
4
5
40
35
30
25
20
15
10
5
Effective pressure scenario (% of overburden)

**Figure 10.**

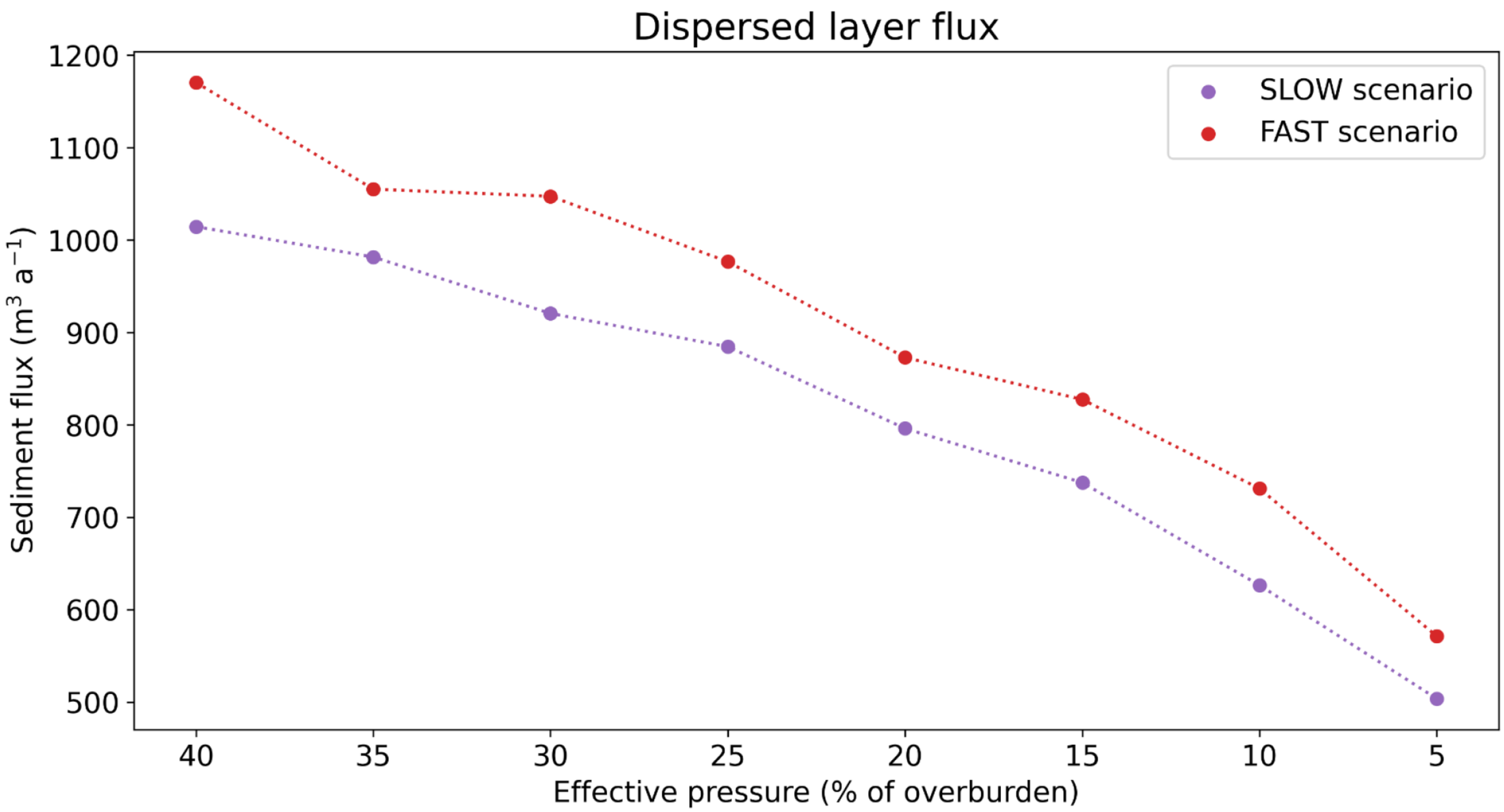
Dispersed layer flux
SLOW scenario
FAST scenario
Sediment flux (m$^3$ a$^{-1}$)
1200
1100
1000
900
800
700
600
500
40
35
30
25
20
15
10
5
Effective pressure (% of overburden)

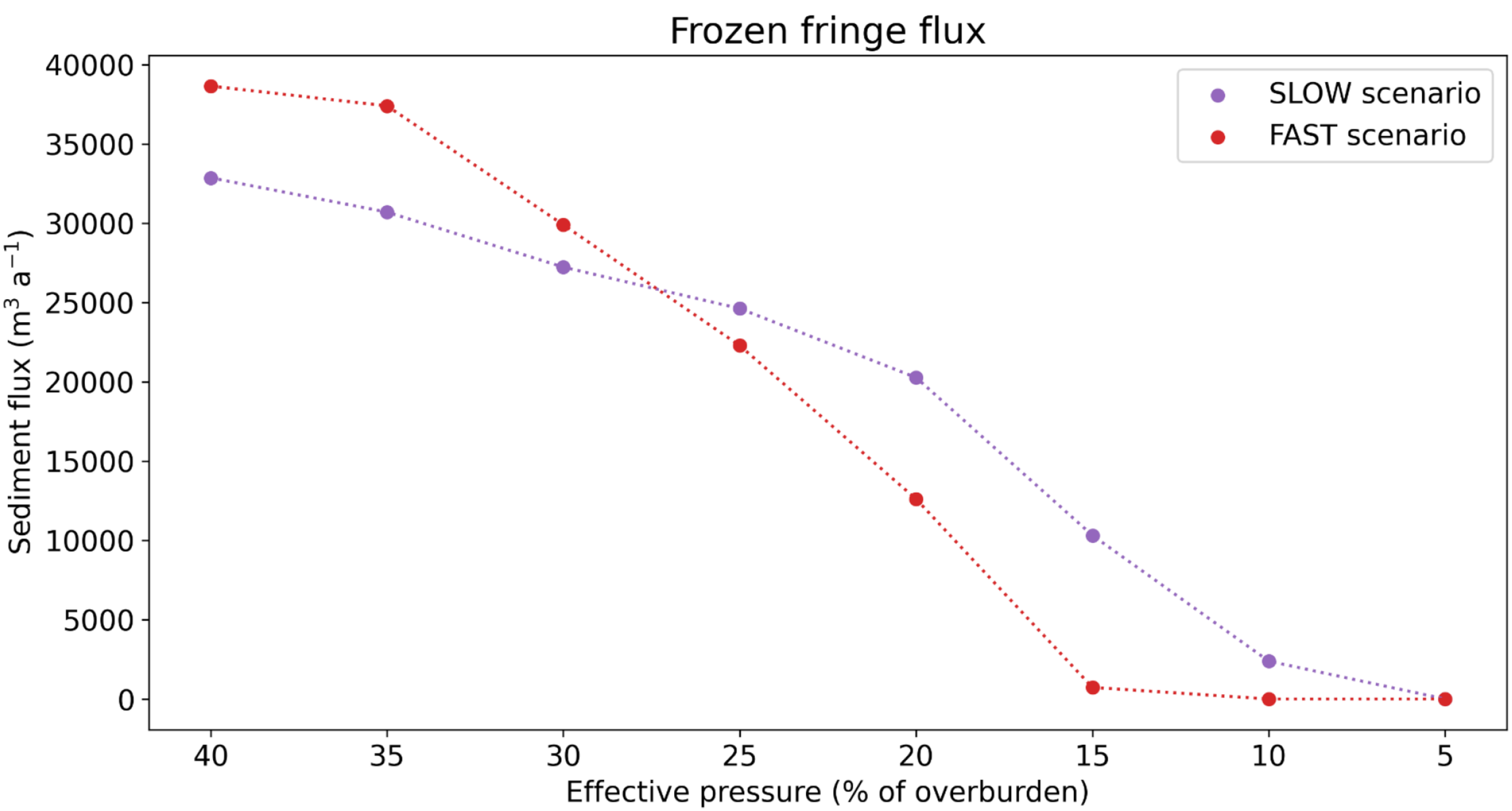
Frozen fringe flux
SLOW scenario
FAST scenario
Sediment flux (m$^3$ a$^{-1}$)
40000
35000
30000
25000
20000
15000
10000
5000
0
40
35
30
25
20
15
10
5
Effective pressure (% of overburden)

**Figure A1.**

# *Fast* scenario, frozen fringe thickness (m)

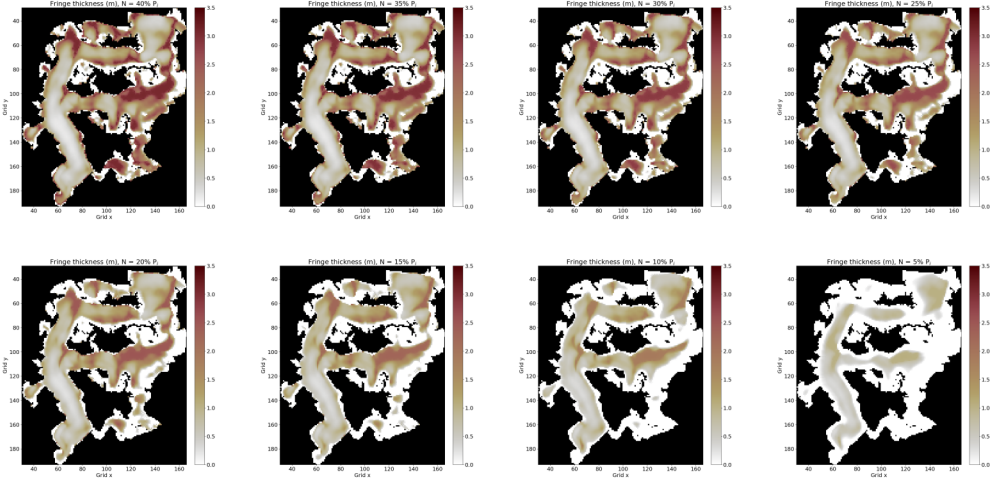

**Figure A2.**

# *Fast* scenario, dispersed layer thickness (m)

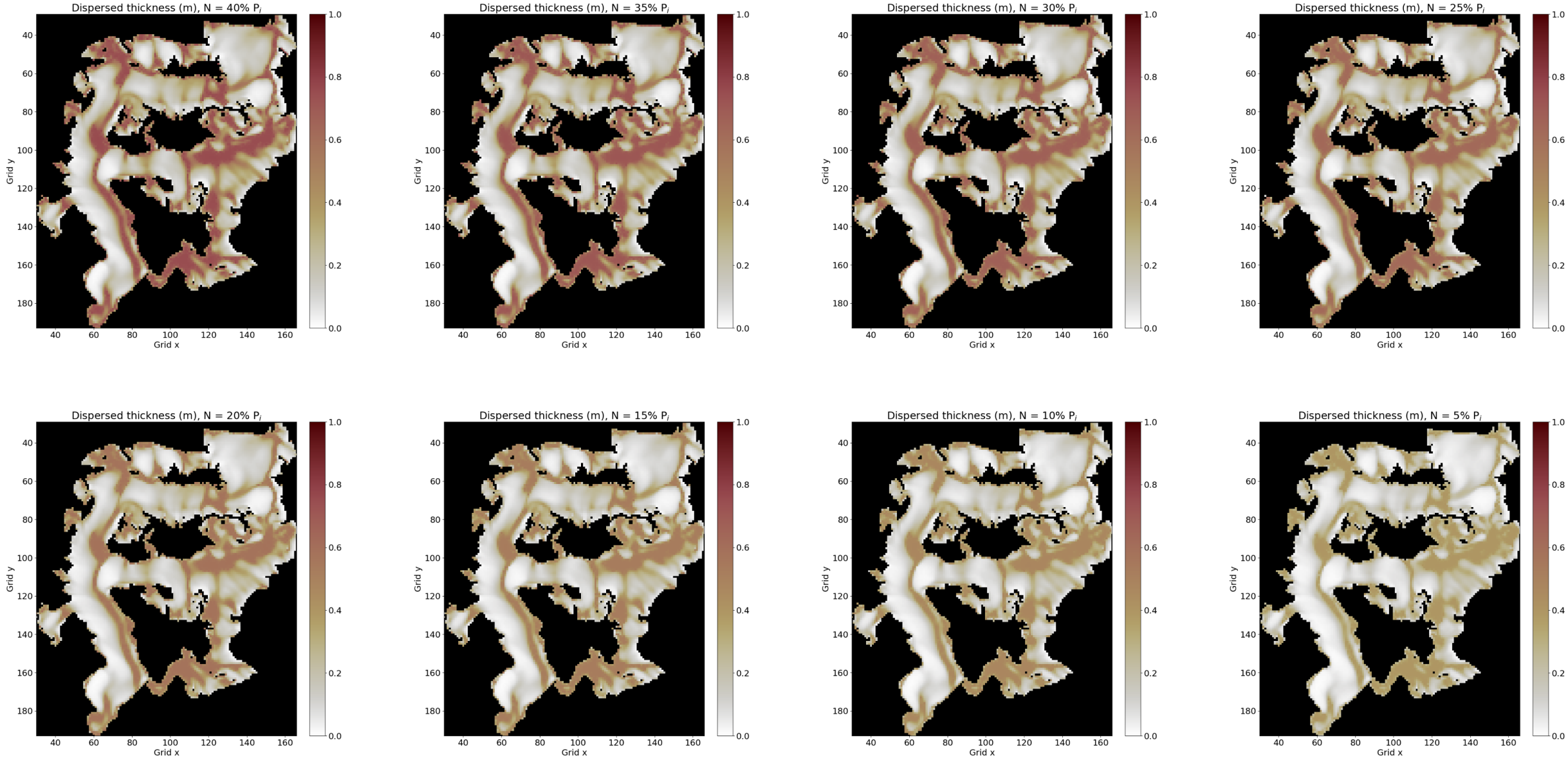

**Figure A3.**

# *Slow* scenario, frozen fringe thickness (m)

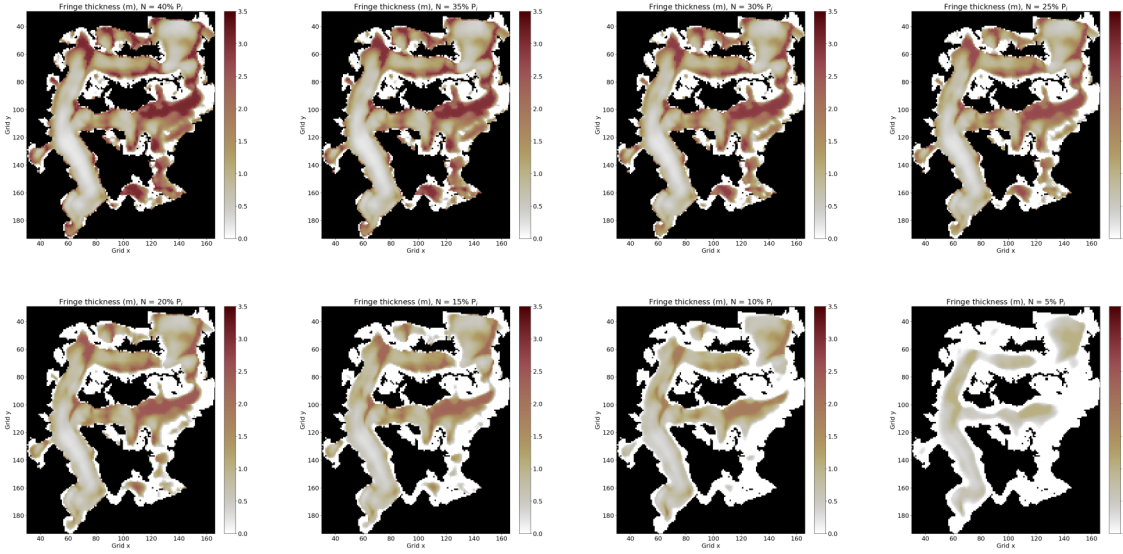

**Figure A4.**
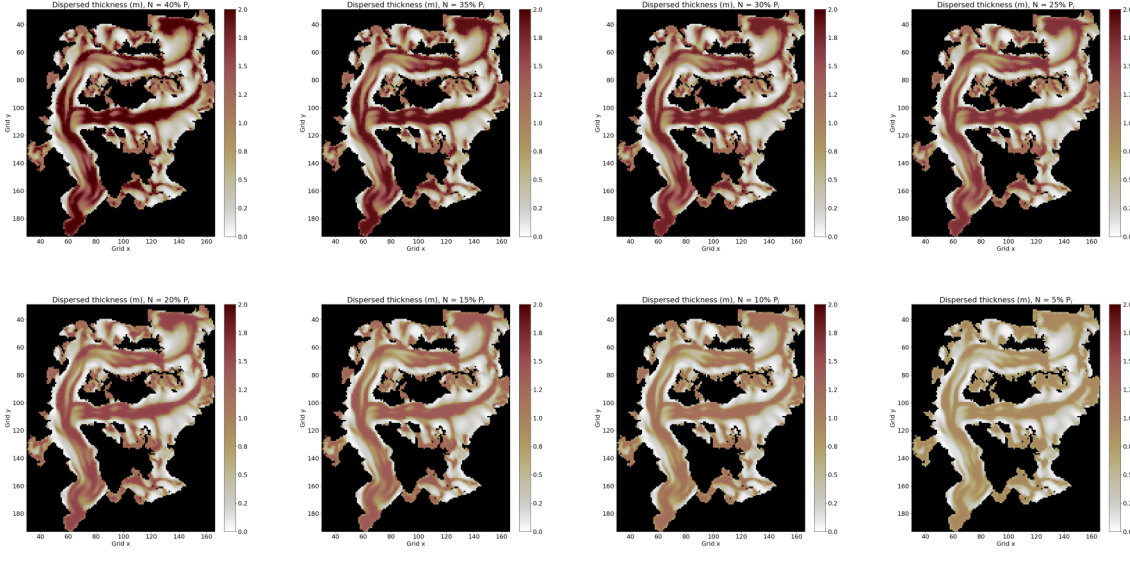
# *Slow* scenario, dispersed layer thickness (m)